UNIVERSITY OF OKLAHOMA

GRADUATE COLLEGE

MODELING AND MEASUREMENT OF SOUND TRANSMISSION IN THE BABOON EAR

A THESIS

SUBMITTED TO THE GRADUATE FACULTY

in partial fulfillment of the requirements for the

Degree of

MASTER OF SCIENCE

By

BROOKE M. HITT
Norman, Oklahoma
2017

MODELING AND MEASUREMENT OF SOUND TRANSMISSION IN THE BABOON EAR

A THESIS APPROVED FOR THE
STEPHENSON SCHOOL OF BIOMEDICAL ENGINEERING

BY

_____
Dr. Rong Gan, Chair

_____
Dr. Vassilios Sikavitsas

_____
Dr. Harold Stalford

The time and effort behind this thesis is dedicated to my partner Justin, for being my light, and to my parents, for their steadfast support in all that I do.

Acknowledgements

First and foremost, I would like to thank my advisor Dr. Gan not only for her leadership these past three years of undergraduate and graduate research, but also for her inspiration as a strong role model for every woman in a male-dominated field. Next, I would like to thank the University of North Texas for allowing us to use their micro-CT scanner and Don Nakmali for traveling to oversee the scans being performed and monitoring the laser Doppler vibrometry experiments. I would also like to thank Trent Briscoe for his work with the newborn tomographic images in creating the initial rough 3D reconstruction of the newborn baboon.

This work was made possible by the National Baboon Research Resources at the University of Oklahoma Health Sciences Center (OUHSC) and was supported by NIH Grant Number R01DC011585.

Table of Contents

List of Tables

List of Figures

Abstract

While many animal models exist for middle ear research, the progression of knowledge is hindered by the impossibility of in vivo investigation in cadavers and the great physiological differences of the distantly related species of current animal models. Pediatric and age-related auditory research could be particularly valuable in the effort toward alleviating the enormous fiscal burdens of both middle ear infections in young children and hearing loss in both the young and elderly communities. The goal of this thesis is to provide steps toward the first nonhuman primate model for auditory research and begin the foundation for the role age plays in sound transmission through the primate ear.

Micro-Computed tomography images were used to digitally reconstruct three-dimensional models of one adult and one newborn baboon middle ear, and dimensions were gathered for key tissue components. The adult elliptical tympanic membrane is 0.77 mm greater along the major axis than in the newborn baboon, while it is 0.61 mm smaller along the minor axis, 0.56 mm less deep in conic shape, and ~ 15 μm thinner. The adult ear canal opening was 0.84 mm larger in height and 0.38 mm larger in width. While the adult middle ear cavity was 1.56 mm greater in height, it was also 2.79 mm smaller in the anterior-posterior direction of the skull. Orientation of the ossicles within the middle ear cavity also differed between the adult and newborn baboon ears; the newborn TM was 31.3° more angled from horizontal and the newborn stapes was 14.4° less angled from horizontal. Next, finite element method was employed to analyze the fluid and structural dynamics of sound transmission through the ear canal at different frequencies. Finally, displacement at the umbo of the tympanic membrane was found

using the FE model and validated using laser Doppler vibrometry experimental data for old (N=6) and young (N=6) baboon age groups. Treating the experimental mean as the accepted value and the FE results as the results to be compared, this gives a percent error of 21.7% at 200 Hz, 12.5% at 1200 Hz, and 24% at 10000 Hz for the newborn model and 30.7% at 200 Hz, 28.5% at 1200 Hz, and 105% at 10000 Hz for the adult model. Displacement values at very high frequencies deviated most from the experimental mean, and overall the shape of the FE curve is similar to that of the experimental curve. Possible limitations of these analyses include: 1) Each FE model was based on one temporal bone, each coming from a different sex; 2) Because no baboon research exists, human mechanical property values were used for analysis. While the FE models seem to be good representations of their corresponding age groups, further improvements can be made. Based on these preliminary results, age does seem to play an impact in sound transmission for baboons, with TM mobility increasing with age.

Chapter 1: Introduction

1.1 Background: Middle Ear Anatomy and Function

1.1.1 Baboon Model

The baboon is one of the largest non-hominoid members of the primate order. It is considered an African and Arabian Old World monkey belonging to the genus *Papio* [1]. Baboons are closely related to humans and have provided significant research benefits to humans in the past. In addition to being primarily bipedal primates, many of the baboon's anatomical structures are analogous to those of the human and their ages can be correlated to human ages on a 1:3 scale. For example, a 5 year old baboon is considered to be at the same stage in its life cycle as a 15 year old human. A baboon raised in captivity can live approximately 30 years, which aligns nicely with a healthy human living approximately 90 years [1]. Furthermore, the hearing range of the baboon is 0.4-30 kHz, making it comparable to that of the human, which is 0.3- 20 kHz.

For most biomedical research an in vivo model is impossible for ethical reasons, necessitating the use of an animal model. Due to the often invasive nature of in vitro investigations, human research is generally limited to cadaver samples. For auditory research, these samples have the further limitation of being sourced predominantly from the older generation of citizens, who are significantly less likely to have healthy hearing, harming their candidacy for being a control case of healthy adult human hearing [2]. An animal model such as the baboon also allows the opportunity for an age analogy to be drawn between a human pediatric model and young nonhuman primate model. Understanding the effects

of age on the auditory system can be important for investigating childhood hearing impairment and the leading cause worldwide for pediatric illness: middle ear infection (otitis media), which costs the healthcare system billions of dollars per year in the United States alone [2].

The baboon model has been used for investigations in physiology and pathophysiology, as well as radiopharmaceutical techniques. In addition, Fourier phase analysis in radionuclide ventriculography, hemodynamic reactions in a septic shock model, and investigations in conjunction with local anesthetics (e.g., effects on cerebral blood flow) are typical examples of research that have been or are currently being performed on the baboon [1]. Recently, baboons have even been considered for stem cell based therapies in the search for a cure for Parkinson's disease [3]. Institutes using the baboon model must be equipped with all instruments and operating facilities as would be needed for investigations in human beings. Ethical considerations must be regarded strictly and supervised by an ethics committee. Protocols must determine exactly why in vivo experimentation is preferred to in vitro tests. Anesthesia techniques in a baboon model allow study on the animal itself, eliminate pain and stress to the animal, and are designed so as to not interfere with the aims of the investigation being performed. Finally, the baboon model is a preferred animal model in biomedical research in fertility, uterine receptivity, and embryo implantation [4,5].

Despite the extensive research done in the baboon skull, little to no literature exists on baboon middle ear biomechanics. Non-human primate ear research has been primarily limited to ototoxicity studies, otoacoustic emissions,

ionomeric prosthesis implants, and a select few publications on immunocytochemical colocalization in the cochlear nuclei [6,7,8,9,10]. Publications discussing the specifics of the auditory system, especially middle ear anatomy, are not present for baboons of any age.

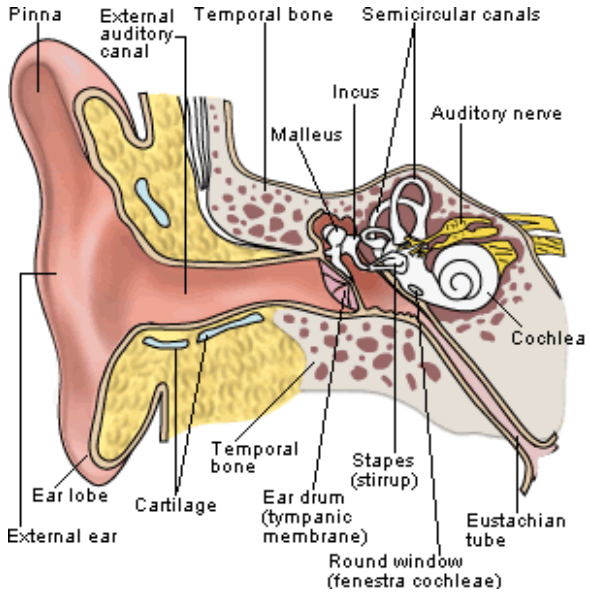

Figure 1. Established structure of the human ear. [Southwest Educational Development Laboratories].

Like in the human, the baboon ear structure is comprised of the pinna (visible outer ear cartilage) and a fleshy ear canal that leads to the first step in sound transmission, the tympanic membrane (TM) and the surrounding annulus. As shown in Figure 1, on the medial side of the TM is the soft tissue manubrium, which attaches the TM to the ossicular chain consisting of the three smallest bones in the primate's body: the malleus, incus, and stapes. These bones are separated by joints and are suspended in the middle ear cavity by seven suspensory ligaments. Unlike many small mammals commonly used in ear research such as the chinchilla, the baboon's malleus and incus are not fused and

are thus more similar to those of a human [11]. The Eustachian tube's primary function is to drain middle ear fluid and keep the middle ear pressure at atmospheric levels. In the inner ear, the cochlea houses the organ of Corti, which is comprised of the basilar membrane on which mechanosensory hair cells reside. The middle ear cavity encloses the TM and ossicular chain and the stapes footplate fills the cochlear opening, the oval window, where it provides the final link between sound waves and the cochlear hair cells that send messages to the brain to produce the sensation of hearing.

1.2 History of Middle Ear Biomechanics Research

Middle ear research, although devoid of a non-human primate model, is extensive and ranges from insects to human cadaver ears. Biomechanics of healthy middle ear structures have been investigated in chinchillas, guinea pigs, and even katydids [12,13,14]. Mechanical properties such as stiffness of diseased middle ears have been discussed in chinchillas, guinea pigs, ruminants, and dogs [15,16,17]. The healthy stapedial annular ligament (SAL) has been reported on in humans, while the diseased SAL has been reported on in chinchillas and other animals [18,19]. Histology focusing on the TM, stapedial annular ligament, and round window membrane has been published in humans and animals such as horses, chinchillas, guinea pigs, and human ears [13,18]. Auditory brainstem response, which requires a living subject (i.e. animal model), has also been studied in chinchillas and guinea pigs. Furthermore, many studies have been done on cadaver temporal bones and chinchillas to investigate how pressure waves

("sound blasts") common in military scenarios affect the middle ear soft tissues to cause hearing damage [20,21].

1.3 Finite Element Method

Among the many approaches taken to gain understanding of ear anatomy and sound transmission, one of the most valuable involves 3D reconstruction of the middle ear followed by finite element analysis. Over the past two decades, the human finite element (FE) model has crucially assisted in the understanding of the intrinsic workings of the human middle ear [22]. Finite element method allows researchers to take a complex geometry and split it into smaller elements, both simplifying the problem for the researcher and the computer and allows greater precision. Commonly used in mechanical engineering applications, finite element (FE) method has been applied to many biomedical research situations in both human and animal models ranging from eyes to dental implants [23,24].

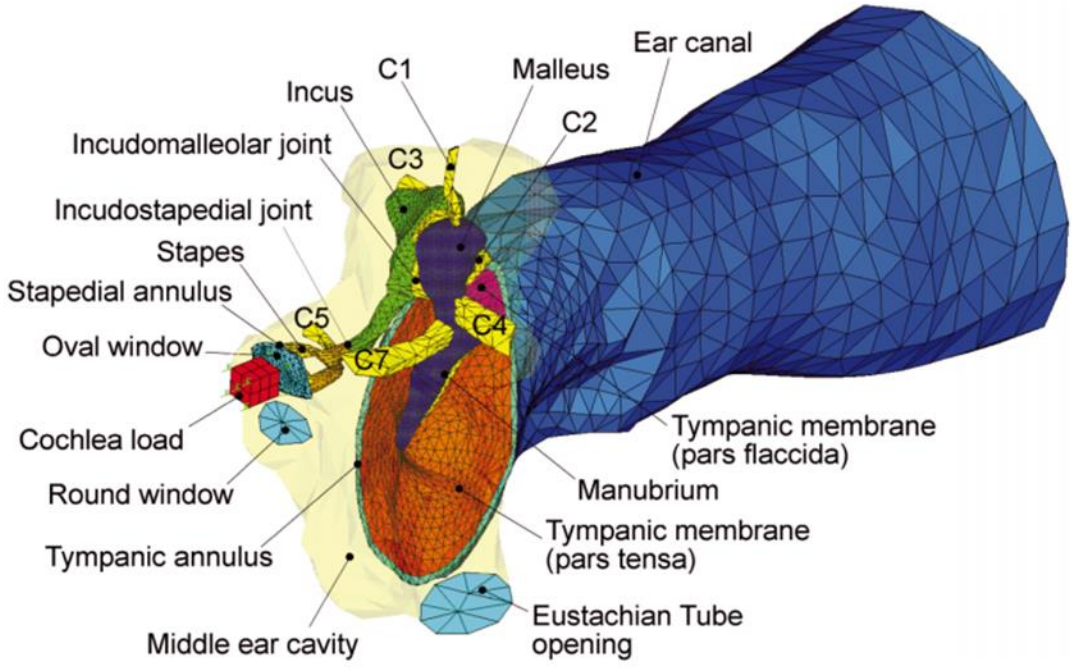

Figure 2. Human finite element model of middle ear cavity with canal. [Gan et al, 2004].

In 2004, a finite element model of the human ear was developed in the Biomedical Engineering Laboratory at the University of Oklahoma in Norman, OK. This geometry has been well-published and has been implemented in the investigation of ear response to numerous conditions, the most common being military blast scenarios. The model was constructed based on a complete set of histological section images of a left cadaver temporal bone in 2004 and was validated by comparing model-predicted displacements of the stapes footplate and TM with published experimental measurements on human temporal bones [25]. This geometry was the basis for the first finite element model of the human ear that featured acoustic-structure coupled behavior between the ear canal air column and the TM and middle ear ossicles with the air in the middle ear cavity. As

shown in Figure 2, this geometry featured the fluid domains of the ear canal and ME cavity, the structures of the TM and the TM annulus, the middle ear ossicles and associated soft joints and suspensory ligaments, and the cochlear load, which modeled a 20 GΩ impedance applied to the stapes footplate.

Three years later, the same research group applied a hyperelastic material model to the TM and important suspensory ligaments and middle ear pressure effects on static and dynamic response of the ear was calculated [26]. That same year, a simplified two-chamber straight cochlea with basilar membrane was introduced to the model and sound transmission from the ear canal into the cochlea was predicted [27]. This human model produced satisfactory agreements between predicted basilar membrane motion and experimental data in literature. This study was the first step toward the development of a comprehensive FE model of the entire human ear for acoustic-mechanical analysis. Another study altered TM geometry to include different numbers and sizes of perforations at particular locations, and the TM displacement and middle ear pressure were calculated. Cadaver ears were perforated similarly and TM displacement was measured by laser Doppler vibrometry. Across frequency ranges, the human FE model was found to accurately predict TM vibrations and middle ear pressure levels when compared to experimental measures [28]. In a later iteration of the human FE model, viscoelastic material properties and a three-chamber spiral cochlea were introduced. This study showed the model's capability of modeling energy absorbance in normal ears and ear with otitis media, otosclerosis, and

ossicular chain disarticulation [29]. The model has also been implicated in evaluating totally implantable hearing systems [30].

During the last thirteen years, the human finite element model has been developed and advanced while proving to be a valuable tool when used in conjunction with experimental data. The model is capable of predicting ear function from canal to cochlea, various modes of ear damage and disease, and even the behavior of implantable biomechanical systems. The analyses discussed above were conducted in ANSYS APDL and investigated ear function in low-pressure conditions in the hearing frequency domain. Similar to the introduction of the human finite element model in 2004 which paved the way for the countless studies in hearing research that followed, this thesis introduces the first comprehensive three-dimensional model of the baboon ear, both for a newborn and adult animal.

1.4 Objectives

By creating and studying a finite element model of the baboon ear, the similarities and differences between humans and baboons can be further evaluated and elucidated. Furthermore, comparing the models of young and adult baboons can serve as a first step toward a nonhuman primate model for use in crucial pediatric auditory health research. Finally, the work in this thesis aims to garner a greater understanding of the biomedical benefits baboons can provide to ear research with the goal of promoting human health and quality of life.

1.4.1 Outline

Computer 3D reconstruction of baboon middle ear

- Micro-CT images are collected for newborn and adult middle ears.
- FEI Amira is used to make labels on the cross-sectional tomographic images before stacking them into a 3D model.
- Using Altair HyperMesh, the 3D models are converted into finite element models where ligament and tendon boundary conditions are applied.

Sound transmission modeled, analyzed, and verified

- Each model is transferred into ANSYS Workbench where the fluid and structural components are divided into analysis software Fluent and ANSYS Mechanical, respectively.
- Appropriate boundary conditions, material properties, and fluid-structure interfaces are applied.
- FE model umbo displacement results are compared with experimental laser Doppler vibrometry data.

Chapter 2: Methods

2.1 3D Reconstruction

2.1.1 Sample Preparation

Two animals were utilized in the scope of this project. The first was a male baboon who was stillborn due to natural causes not related to any part of the head. Based on the 1:3 accepted baboon to human age ratio, this newborn baboon is considered to be equivalent in age to a human child aged 0-3 years old. The

second was a female baboon who also died of natural causes at 11 years old due to a bowel disorder. This adult baboon is considered to be equivalent in age to a human adult aged approximately 33 years old. Both baboon samples are from the National Baboon Research Resources at the University of Oklahoma Health Sciences Center (OUHSC) in Oklahoma City, OK. At the National Baboon Research Resources center, the animals were evaluated post-mortem and the skulls with epithelial tissues intact were packed in ice for transit to Stephenson Technology and Research Center in Norman, Oklahoma.

2.1.2 Micro Computed Tomography

Micro Computed Tomography, also called micro-CT, is similar to traditional medical Computed Tomography (CT) scanners found in hospitals and major medical centers. According to the National Institute of Biomedical Imaging and Bioengineering, computed tomography is a computerized x-ray imaging procedure in which a narrow beam of x-rays is aimed at a patient and quickly rotated around the body, producing signals that are processed by the machine's computer to generate cross-sectional images—or "slices"—of the body. See Figure 3 for an example. These slices are called tomographic images and contain more detailed information than conventional x-rays.

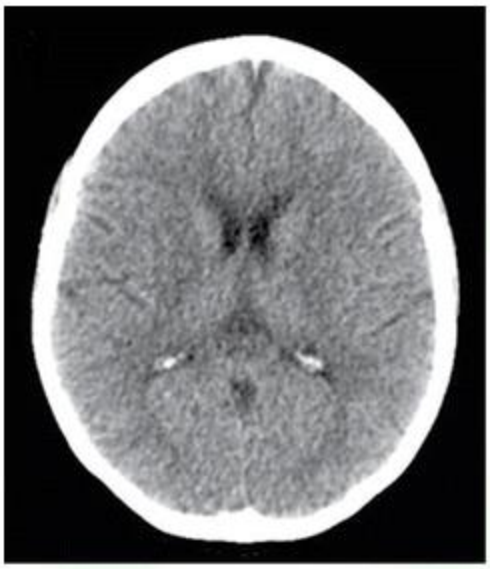

Figure 3. Example of typical CT scan tomographic image of the human brain inside the skull. [Ginat and Gupta, 2014].

While typical CT scanners for medical care have an image resolution of 1-2 millimeters, micro-CT scanners have a resolution on the scale of micrometers (μm). This means that a micro-CT scanner will be able to capture structures less than 1-2 millimeters that would not be visible in a traditional CT scan. The human tympanic membrane, for example, is 50-100 μm in thickness and would thus not be visible in a CT scan [31]. However, because of the higher resolution, a micro-CT scan also delivers a higher dose of radiation to complete the scan, so micro-CT is rarely done on humans or live animals [32]. Isolated temporal bones such as the ones in this study, on the other hand, are not in danger of being damaged by a single incidence of the micro-CT scan.

In a micro-CT scan, X-rays are generated by a micro-focused X-ray tube, which uses a beam of electrons accelerated by a voltage of up to 240 kV (or more in a vacuum tube), and are focused onto a metal target. The interaction between

the fast moving electrons and the metal target is responsible for creating X-rays. The energy delivered to the sample during the scan, or the X-ray voltage, highly depends on the type and material composition of the sample. The most optimal material discrimination is usually obtained by using lower voltages. However, in the case of dense materials, the penetration value (the percentage of detector counts around and through the sample) might be too low, causing noise and "artifacts" [37].

Beam hardening is the most common micro-CT artifact, and occurs when the X-ray beam comprising a range of energies encounters differences in absorption from different angles and along different paths through the object, either due to a high density of the object as a whole or due to disproportionately dense segments of an object. Different X-ray paths result in varying absorption of the easily-absorbed low-energy X-rays. This can result in either "cupping" artifacts in dense objects (brighter regions around the edges of the material) or "streaky" artifacts in denser sections of a larger object (especially for very dense parts, such as metal tags) [37]. Taking all of these factors into consideration, different scans call for different X-ray voltages to be applied. For reference, biological samples are generally scanned at 30 to 100 kV, small rocks and light metals are often scanned at 60 to 150 kV, and heavy metals are often scanned at 160 to 240 kV [37]. After the scan is performed, image filters are generally applied to allow the user to adjust the contrast, noise, and lighting of the picture in a process called thresholding.

Micro-CT data can be visualized in two different ways, either by volume rendering or surface rendering. Volume rendering is typically conducted in 3D data analysis software and involves iso-surface views using a user-defined threshold value, or a user-defined greyscale gradient for more advanced 3D rendering algorithms. These differ from 3D Computed Aided Design (CAD) software in that they handle full voxel data, i.e. the data exists throughout a 3D voxel grid, not only on surfaces of the object. In other words, CAD software packages use triangulated mesh data of surfaces only (point locations), while full CT data comprise of data at every point in 3D space with a grey value at every point. Therefore, a volumetric dataset like the ones used in this thesis is significantly larger and requires more intensive computing power, even for simple visualization [37].

On February 12, 2016 the baboon temporal bones were transported to The University of North Texas in Denton, TX, where a SkyScan 1172 Micro-CT scanner was employed to obtain tomographic images of each sample. A total of 1260 cross-sectional images were collected of the newborn baboon ear, while 1315 images were collected for the adult baboon ear. Because of the advanced technology of the SkyScan 1172, the images have a resolution of 9 μm per pixel and were taken at an approximate distance of 9.91 μm between each slice. The micro-CT scans performed in this thesis involved X-ray energy of 90 kV and a current of 110 μA. See Figure 4 for examples of the great detail this machine was able to achieve for the smallest bones in the body.

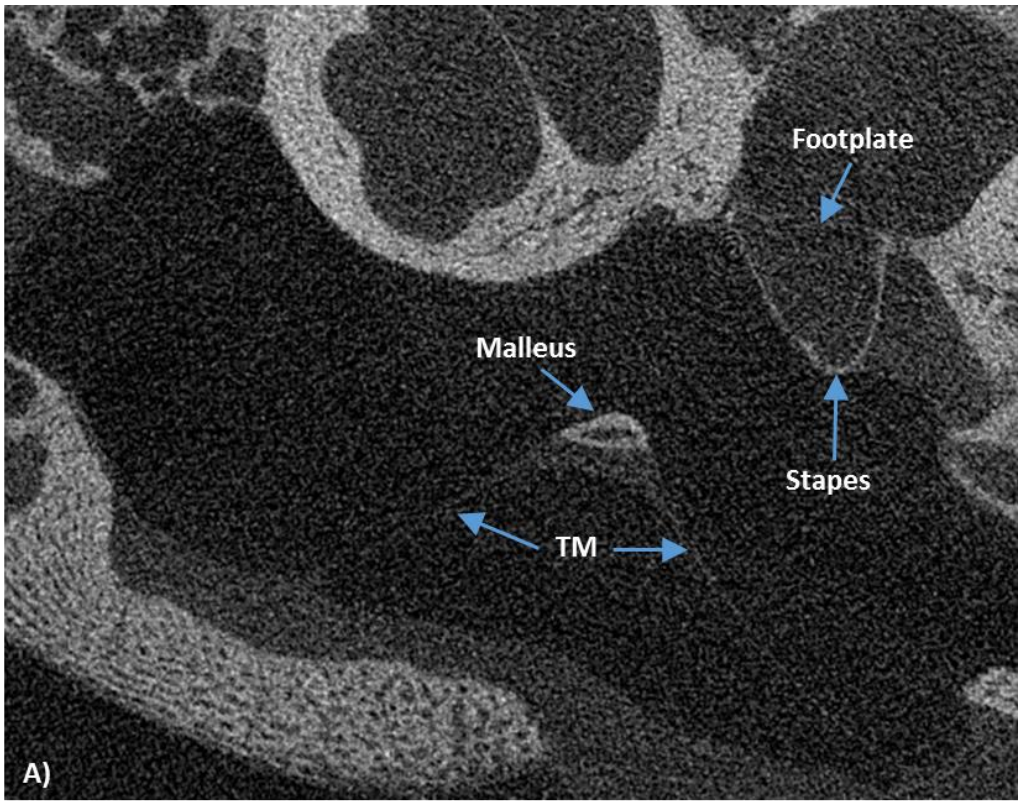
Footplate
Malleus
Stapes
TM
A)

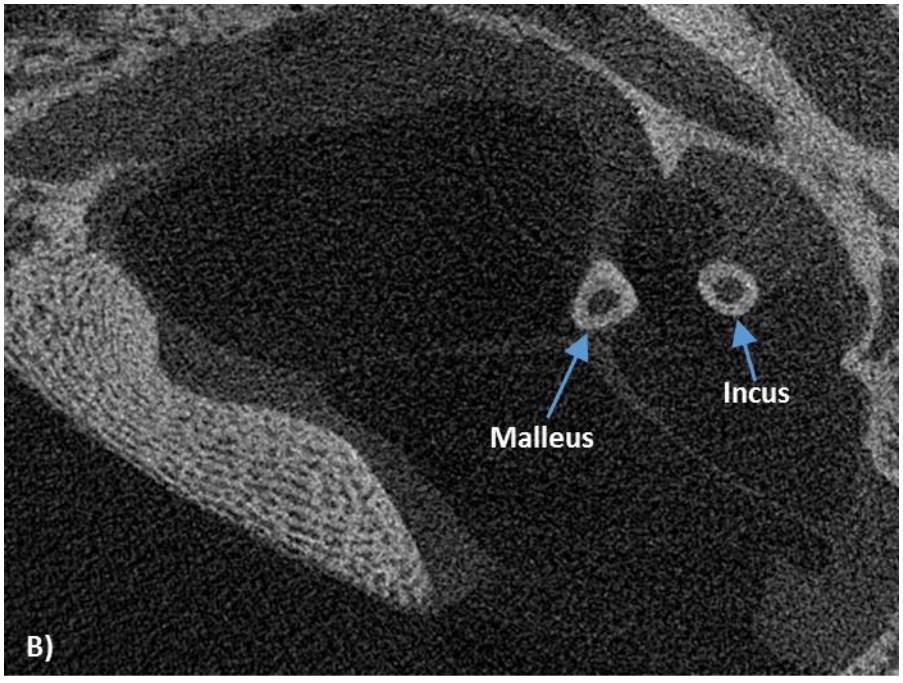
Incus
Malleus
B)

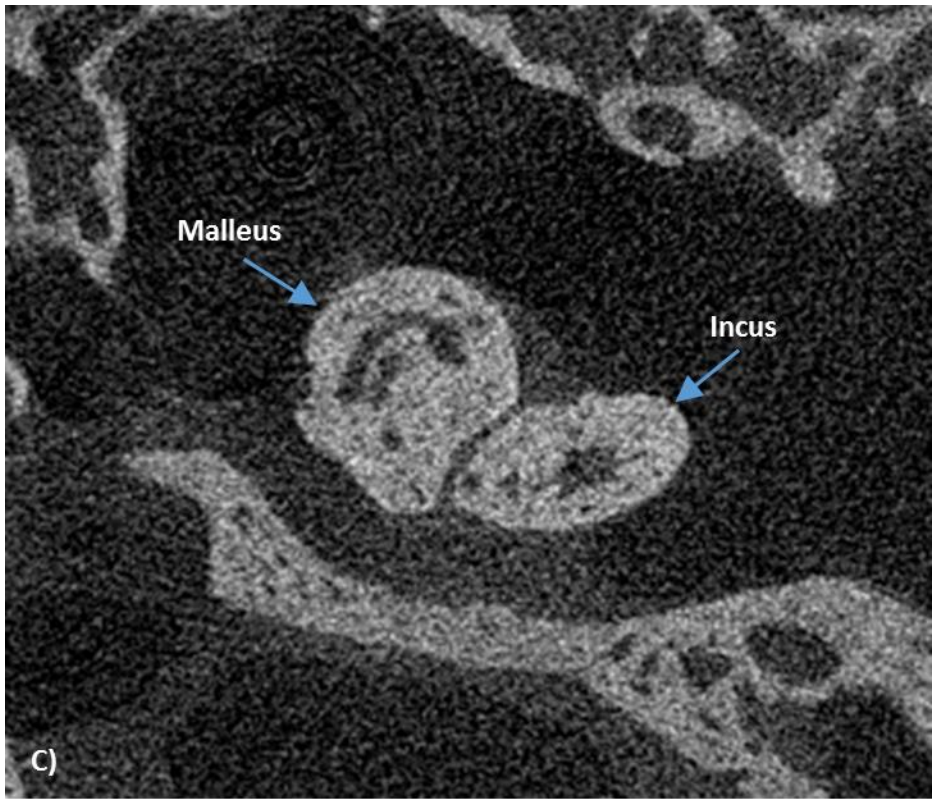

Figure 4. Tomographic images from micro-CT scanner of newborn baboon ear demonstrating how structures were identified.

In the tomographic images from the scan, structures varied from black to white depending on material density and user-determined thresholding values. Grey-scale thresholding allowed structures with grey values less than a specified value to show up as white and not be visualized, while structures with values greater than a specified grey value would be visualized as black. For example, if these two thresholding values are set equal, all structures in an image will be either white or black and there will be no grey.

In order to determine greyscale thresholding for the baboon models, visibility of the TM and its thickness was considered. According to optical coherence tomography (OCT) and surgical dissection performed within this

research group during the scope of this thesis, the adult baboon TM is approximately 25 micrometers in thickness. Because of the 9 micrometer resolution of the scanner, the adult tomographic images were greyscale adjusted in such a way that the TM was displayed in the images as 2 to 3 pixels in thickness (18-27 μm). This occurred when the lower limit was set to 16 and the upper limit was set to 147 in Amira's greyscale settings. Anything below 16 in grey value appeared white, while anything above 147 in grey value appeared black. All other structures varied in greyscale according to object density. According to surgical dissection, the newborn TM is approximately 40 micrometers in thickness. When the newborn images were filtered using the same thresholding values used for the adult, the TM was visualized in the images as 4-5 pixels in thickness (36-45 μm), in accordance with the measured newborn TM thickness value.

2.1.3 Developing a 3D Model

FEI Amira is a 3D software platform that allows scientists and researchers to visualize, manipulate, and understand data from numerous imaging methods including magnetic resonance imaging (MRIs) and computed tomography scans. Despite the vast potential for many applications, resources emphasizing the applications and instructions for using Amira are lacking. For this reason, this section will be particularly detailed in describing the following method for generating a 3D model using Amira. The procedure below was completed twice—once for the newborn model and once for the adult model. Trent Briscoe,

an undergraduate researcher in the lab in Spring of 2016, performed the initial transition from newborn tomographic images into a rough initial 3D model in Amira. All additional steps toward the finite element models, including transferring the newborn Amira model into HyperMesh and every step in the adult 3D reconstruction process, were performed by the author of this thesis.

At the Stephenson Technology and Research Center at the University of Oklahoma, the tomographic images from the micro-CT scans described above were separately imported into Amira 5.4.1 to construct a 3D geometry of the tympanic membrane, ossicular chain, and middle ear cavity. Then, a maximum of 130 tomographic images were selected for use at a time. Initial attempts involving uploading more than 130 images caused the program to fail. Once the data was loaded into the user interface, colorfield settings were maximized.

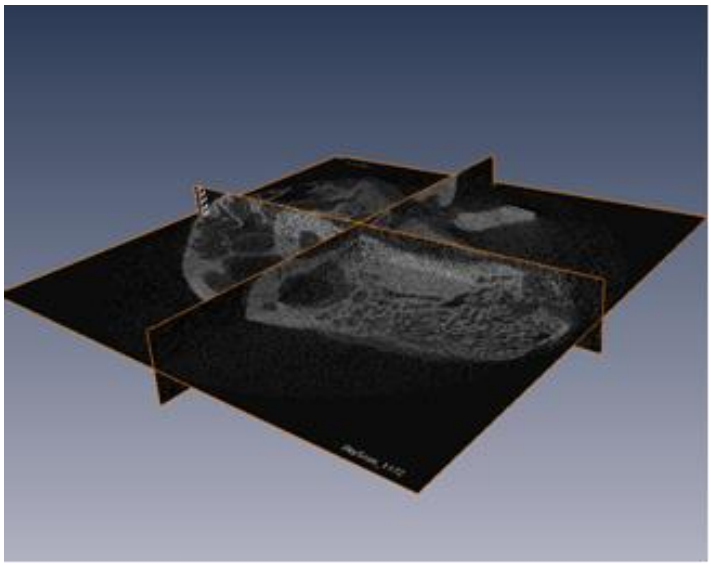

Figure 5. Tri-planar orthoslice view of portion of the baboon temporal bone in Amira.

Once imported, there are many different options for data visualization or manipulation. These include orthoslices, which allow the user to see the data in the three major planes; image filters, which allow the user to adjust the contrast; noise and lighting of the images; and labelling, which allows the user to select pixels in each picture to add into the 3D model. Orthoslices, exemplified in Figure 5, are useful for gaining a precursory 3D view of the data before any images are segmented or any material is isolated as a part of the model. In a segmentation editor, the user is allowed to view each slice and add or subtract material from the 3D model via the greyscale thresholding technique dicussed in the previous section.

When the data is opened in the Segmentation Editor, the data is automatically zoomed in at a 1:1 concept ratio to the upper left hand corner of the middle data slice. However, this does not adequately show the entire middle ear, even for the smaller newborn temporal bone. In order to adequately model the data, the slide set had to be zoomed out and realigned to be centered on the area of interest. By starting at slide one in each slide set, the tympanic membrane was first modeled by highlighting the TM every ten slides and interpolating between the slides. This created an initial outline of the TM. Then, each slide was adjusted to account for any holes in the data, refine the edges for the 3D model, and ensure that the data matches up with where the TM is actually located. Once the TM was finalized for a section of slides, the selection was added to the material list as its own entity.

After being added to the selection, any islands were removed and the labels were double checked before being smoothed based on the greater 3D visualization of each component with a bias toward smoothing that would result in a continuous final surface. This is the most important step in obtaining a smooth model directly from the tomographic slices to expedite the overall modeling process.

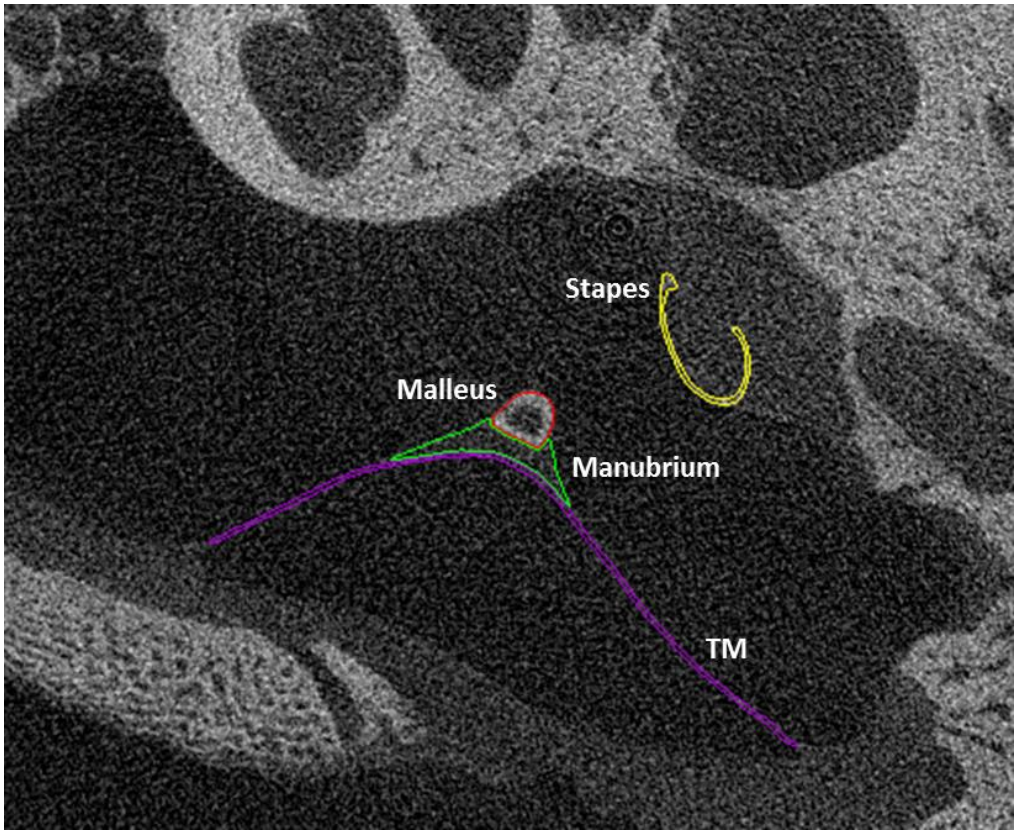

Figure 6. Micro-CT image with the TM (purple), manubrium (green), malleus (red), and stapes (yellow) labelled using Amira software. Image courtesy of Trent Briscoe, 2016.

In order to distinguish between the TM and the other materials that were modeled, including the malleus, incus, stapes, and middle ear cavity, new materials were modeled as different materials each with a unique color as shown in Figure 6. In order to obtain a fully assembled 3D model, each set of 130 slides was used to generate a surface individually with a different color for each structure: purple (TM), green (manubrium), red (malleus), sky blue (incus), navy (ISJ), and yellow (stapes). All of these images were labeled in the same network, but the middle ear cavity outline was created in a separate network so that the middle ear cavity could be visualized separately from the other structures. This later allows for the middle ear cavity to be made semi-transparent, leaving the internal structures visible early in the process when it was important to verify the correct orientation based on the micro-CT images. Once labelling and image segmentation was complete, each set of labels was turned into a 3D structure by stacking each of the labels 9.91 micrometers (distance between the images) apart and interpolating, creating a surface for each component segment.

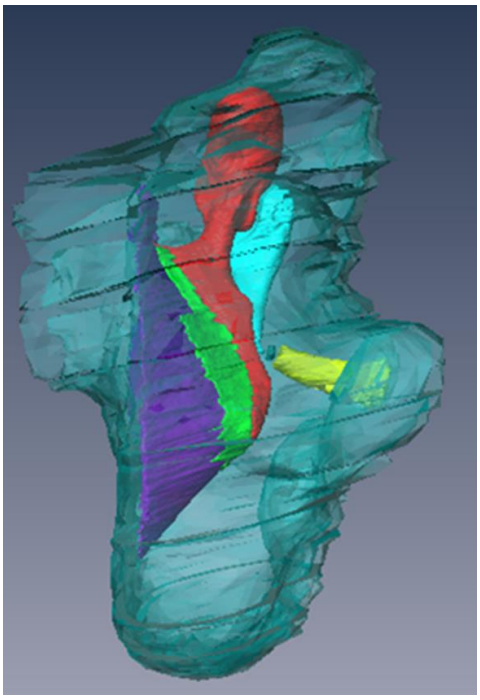

Figure 7. 3D Visualization of newborn middle ear from labelled tomographic slides in Amira software.

Once each surface had been generated, a new network was created exclusively with the surface generations of the middle ear and the middle ear cavity. In other words, the original picture data sets and label files were omitted from this network to simplify the amount of RAM required from the computer, again to ensure the software would run smoothly. The slides had to be realigned as the middle ear cavity and middle ear structures were joined in one network because the middle ear cavity used about 300 more slides than the middle ear model used. A simple translation command was performed to correct this, yielding the visual in Figure 7.

At this point, the surfaces had a high number of faces and thus a high number of edges, meaning it would create a very fine mesh with an enormous number of elements. In order to combat this, each structure's surface generations

were simplified. The faces were reduced from about 2,000,000 faces in each component segment to 1000-2500 faces, which successfully smoothed surfaces while minimizing the file sizes and the number of insignificant elements.

Once the newborn and adult baboon ears were visualized in Amira, key dimensions were measured. These included general heights and widths of each ossicle, the middle ear cavity, and ear canal opening into the middle ear cavity. Due to its elliptical shape in the baboon, TM dimensions were measured along the major axis, minor axis, and depth of conic shape from the center of the TM perpendicular out to the vertex of two lines connecting the outer edges of the TM along the major and minor axis. Furthermore, the angles at which the TM and stapes sit were measured from the horizontal axis determined by the location of ear canal and Eustachian tube openings with respect to the baboon skull, as shown in Figure 8.

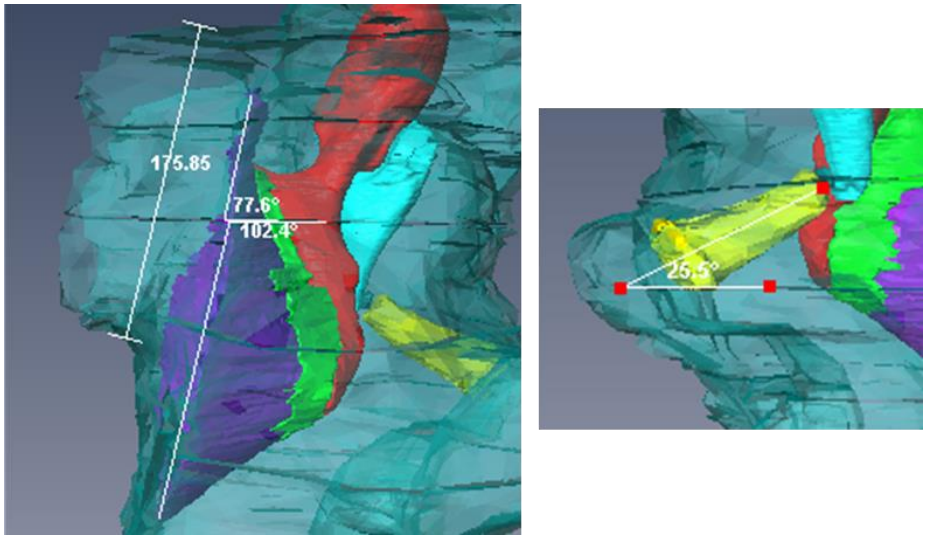

Figure 8. Demonstration of measurement of angle of TM (left) and stapes (right) from horizontal.

2.2 Finite Element Analysis

2.2.1 Constructing an FE Mesh

In order to export the adult and newborn baboon middle ear model networks from Amira into Altair HyperMesh, the AmiraMesh extension needs to present in the Amira license. If the extension is not available, a free trial license including the extension may be requested from FEI. This extension allows the surfaces comprising the network to be exported individually as .hmascii files. These can be directly opened in HyperMesh where the surfaces will automatically be comprised of a finite element mesh. If this were a simple geometry, this would likely be the only step required. However, because each of the surfaces were made in 130 slide segments, the meshes will need to be manually attached to create complete structures such as the ones displayed in Figure 9. For example, if the malleus spanned 450 slides, when the surfaces are imported into HyperMesh, there will be 4 pieces of the malleus that need to be meshed together before proceeding.

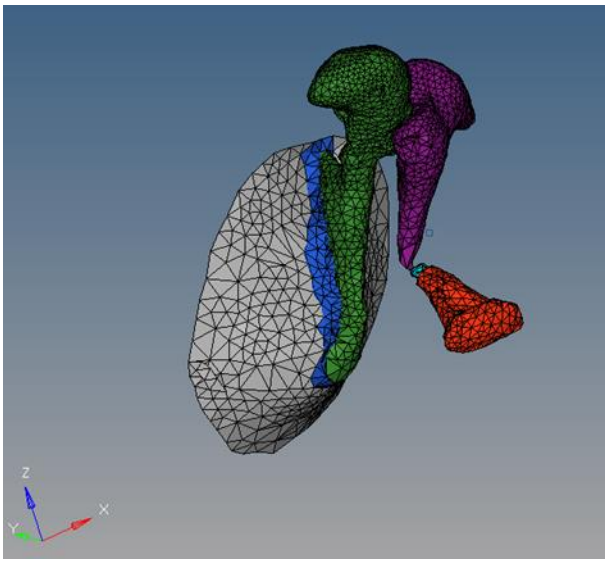

Figure 9. Example of finite element mesh of middle ear structures including ossicles, manubrium, and tympanic membrane.

Once the structures are completely meshed, it must be verified all internal structures have no edges. Each structure needed to have no holes or bad elements because it is only a surface at this stage. In order to create an object with three-dimensional elements, the surface for each structure must be able to enclose volume. The TM, annulus, ossicles, manubrium, joints, and suspensory ligaments greater discussed in section 2.2.2, all need to be tetrahedral SOLID185 elements before being imported into Mechanical APDL. No two-dimensional shell or surface elements should be imported into APDL. Figure 10 depicts how these components were renamed beginning with "mesh_" in order to be compatible with APDL's naming guidelines to ensure the components are correctly identified as 3D meshes. Here, a random material was assigned to each component to avoid APDL reading all the structures in as one component instead of several different components.

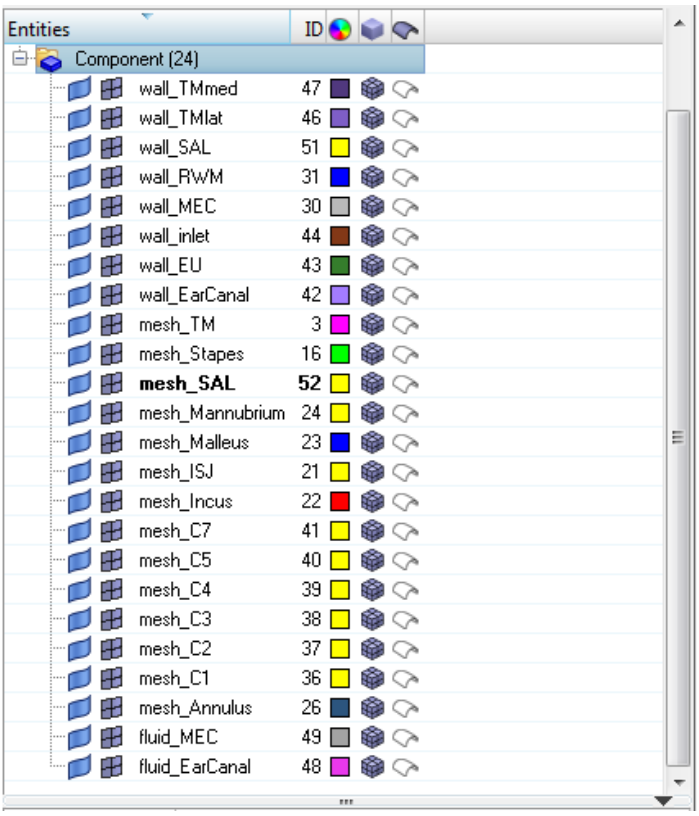

Figure 10. Components list shown in HyperMesh after formatting for analysis. Note: C1-C7 are ligament acronyms used for brevity within our lab. Refer to section 2.2.2 for more detail.

Although APDL may read the HM-derived CDB file (which consists of multiple components, their names, etc.) without issue, External Model in Workbench will only read the mesh of the first component without any other information. To overcome this, the user imported the HM-derived first .CDB file into APDL and generate a second APDL-derived .CDB file to import into External Model. Figure 11 displays the structural meshes in APDL before exporting as a secondary .CDB file.

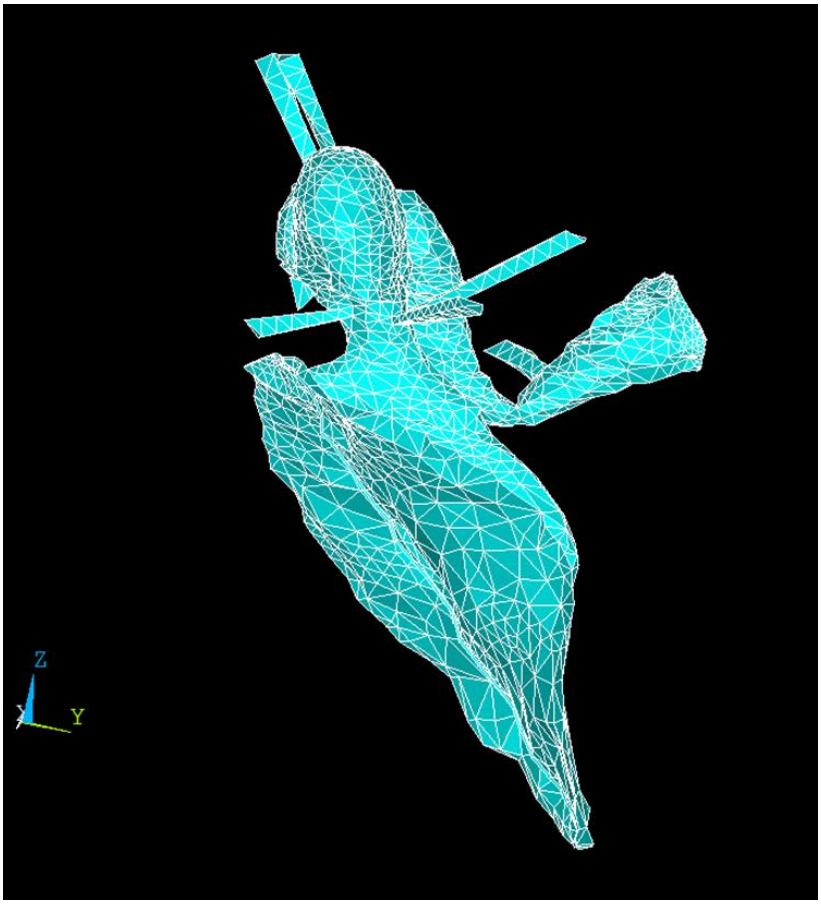

Figure 11. All solid components shown in APDL viewing window.

Next, the APDL-derived CDB file was imported into ANSYS WorkBench through the External Model component system. Using Engineering Data, the correct material properties discussed 2.2.3 were input during this step. Next ANSYS Mechanical was opened to confirm correct importation, which can be seen in Figure 12. From here, each component was assigned its corresponding material set that was entered in Engineering Data. The option for Nonlinear Effects was turned on.

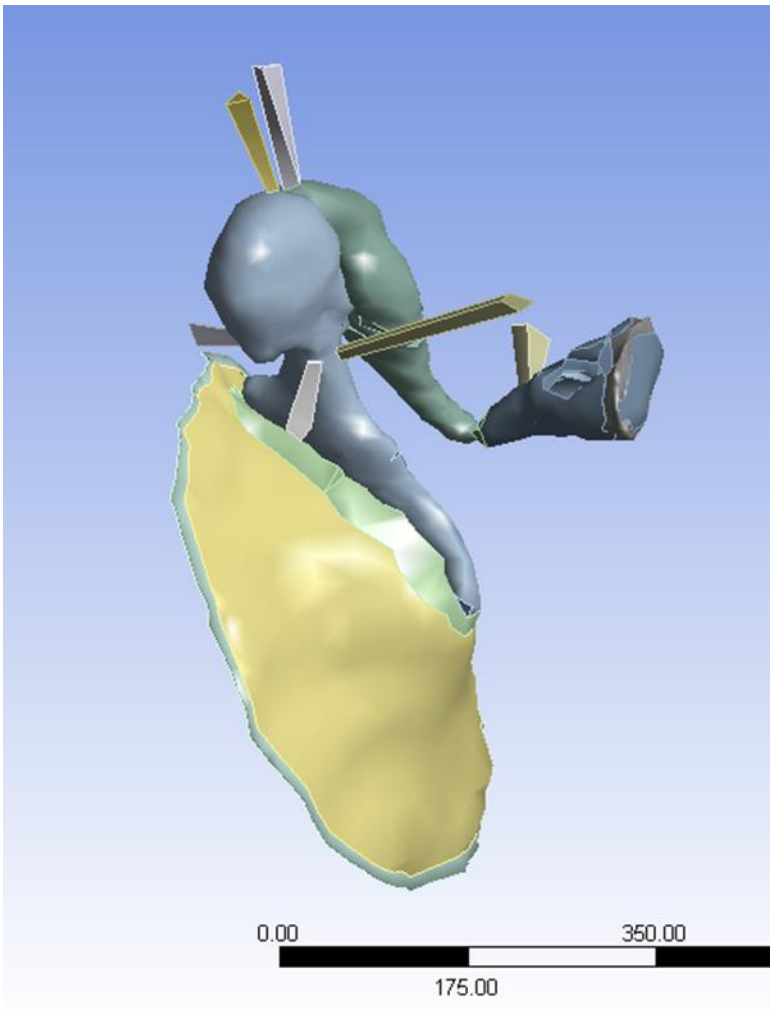

Figure 12. Solid components shown in ANSYS Mechanical.

For the fluid domain analysis, the middle ear cavity (MEC) and ear canal need to be separated and independently three-dimensionally meshed, with all two-dimensional elements deleted. These elements do not need to be assigned a Fluid element type and are named with the prefix "fluid_" as shown in Figure 10. The "wall_" components are called fluid surface interfaces (FSIs) and are the two-dimensional elements that, when combined, completely enclose a fluid domain. Components wall_TMlat, wall_inlet, and wall_EarCanal enclose the ear canal fluid domain. The remaining FSIs, wall_TMmed, wall_SAL, wall_RWM,

wall_MEC, and wall_EU enclose the MEC fluid domain. Wall_RWM is the round window membrane, and the Eustachian tube opening is closed to serve as the FSI wall_EU in this setup.

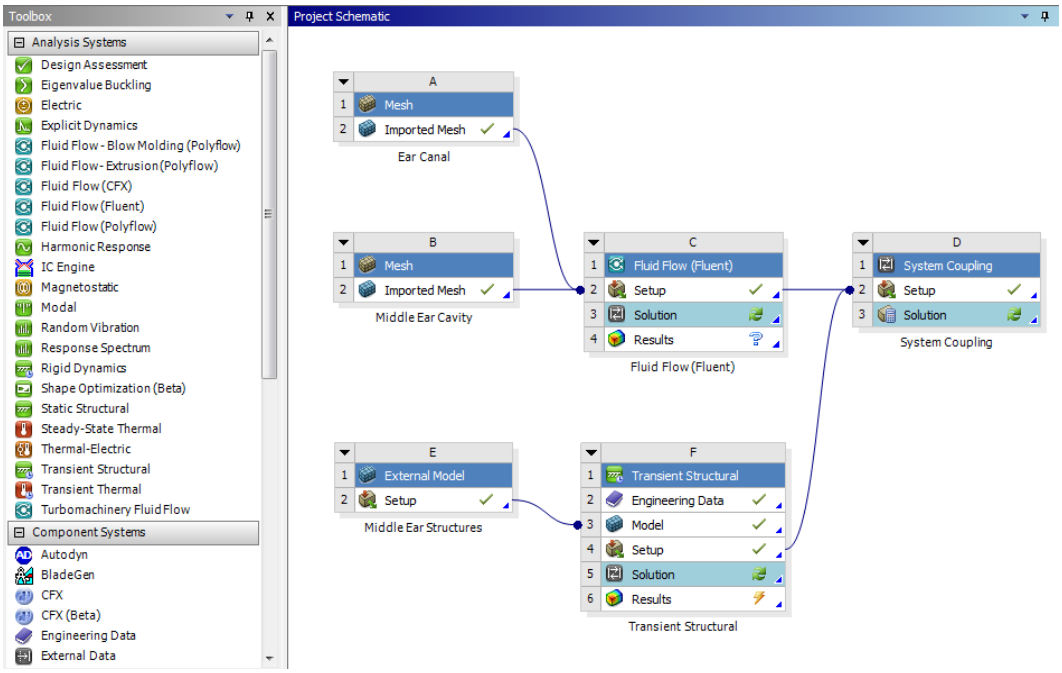

Figure 13.The ANSYS Workbench Project Schematic showing the flow of data from the mesh readers to the analysis systems to the coupling service.

Fluent is a computational fluid dynamics solver that utilizes the constitutive Navier-Stokes equations to predict fluid flow. These equations consist of the continuity and momentum equations that are standard equations solved by Fluent, the energy equation necessary for flows involving heat transfer or compressibility, and the ideal gas law for compressible flows. Effects due to turbulence were not considered here.

The following equation is the 3-D continuity equation, also called the mass conservation equation, and is valid for incompressible as well as compressible flows.

$$\frac{\delta \rho}{\delta t} + \nabla \cdot (\rho \vec{v}) = S_m$$

Here, ρ is the density and $\vec{v}$ is the velocity vector. S_m is a source term representing the mass added from phase change or any user-defined sources [29]; for the FE analyses , there is no source term and S_m is zero.

The momentum equation of a non-accelerating reference frame is described by the following equation.

$$\frac{\delta}{\delta t}(\rho \vec{v}) + \nabla \cdot (\rho \vec{v} \vec{v}) = -\nabla p + \nabla \cdot (\bar{\bar{\tau}}) + \rho \vec{g} + \vec{F}$$

In this equation, p is the static pressure, $\rho \vec{g}$ is the gravitational body force, and $\vec{F}$ is the external body forces [29]. Gravitational effects are ignored, and thus $\rho \vec{g}$ is zero. The pressure waveform applied to the entrance of the ear canal (discussed later) is accounted for by the external body forces. $\bar{\bar{\tau}}$ is the stress tensor and is given by

$$\bar{\bar{\tau}} = \mu[(\nabla \vec{v} + \nabla \vec{v}^T) - \frac{2}{3} \cdot \vec{v}\, I$$

where μ is the molecular viscosity of air, I is the unit tensor, and $\nabla \vec{v}^T$ is the effect of volume dilation [29]. The energy equation is given by

$$\frac{\delta}{\delta t}(\rho E) + \nabla \cdot \left(\vec{v}(\rho E + \rho)\right) = \nabla \cdot \left(k_{eff} \nabla T\right) + S_h$$

where E is energy, k_{eff} is the effective thermal conductivity, and S_h is the source term that contains contribution from radiation and other volumetric heat sources [29] [30]; S_h is zero.

An equation of state is necessary to close the above equations. This is achieved through the application of the ideal gas law for compressible flows; expressed by

$$\rho = \frac{p_{OP} + p}{\frac{R}{M_w} T}$$

where p_{OP} is the operating pressure of the analysis, R is the universal gas constant or 8.314472 (J/mol-K), and T is the absolute pressure computed from the energy equation [28].

To utilize Fluent for this analysis, the user defined the fluid domains' materials and boundary conditions and the fluid domain mesh must be exported as a .MSH file type. To import the fluid mesh, a Mesh component system is dragged into the project schematic by right-clicking on the Mesh cell and selecting Import Mesh File. The search parameters were adjusted to include the .MSH file type otherwise the file would have not been accessible. Then, as in Figure 13, the imported mesh was connected to the Setup cell of Fluent. This figure shows two imported meshes – one for the canal and another for the ME cavity. The Fluent domain was set to transient and pressure-based. Finally, the system is coupled using a System Coupling module to integrate the fluid dynamics and structural dynamics of the system.

2.2.2 Boundary Conditions

While the ossicles, TM, manubrium, and middle ear cavity are all visible in the micro-CT images, key soft structures do not have the size or density to be

visible. This leaves some of the most important factors, the suspensory ligaments, to be modeled in HyperMesh based on notes taken during dissection of the baboon samples. Similar to humans, seven suspensory ligaments and tendons including the SAL are found in the baboon middle ear. The five ligaments begin at a different ear bones and project outward to the bones of the middle ear cavity (MEC), where they hold the middle ear structures in place, as they are not simply floating around in the MEC. Each of the two tendons connects one of the ossicles to a muscle.

As shown in Figure 14, attached to the malleus are superior (C1), lateral (C2), and anterior (C4) ligaments. On the medial side of the malleus is the tensor tympani tendon (C7). The incudomalleolar joint (IMJ) connects the malleus to the incus, which has a posterior (C3) and superior (C1) ligament. Note: The ligaments projecting form the superior of the malleus and incus are considered a ligament group (C1) because of their similar proximities, direction, and mechanical properties. Next, the incus connects with the stapes via the incudostapedial joint (ISJ). The stapes has a posterior (C5) tendon that assists in stabilizing the stapes and can flex when "warned" of louder sounds (higher pressure waves) to help prevent pressure transfer into the cochlea. The stapes is suspended inside the oval window by the circular stapedial annular ligament.

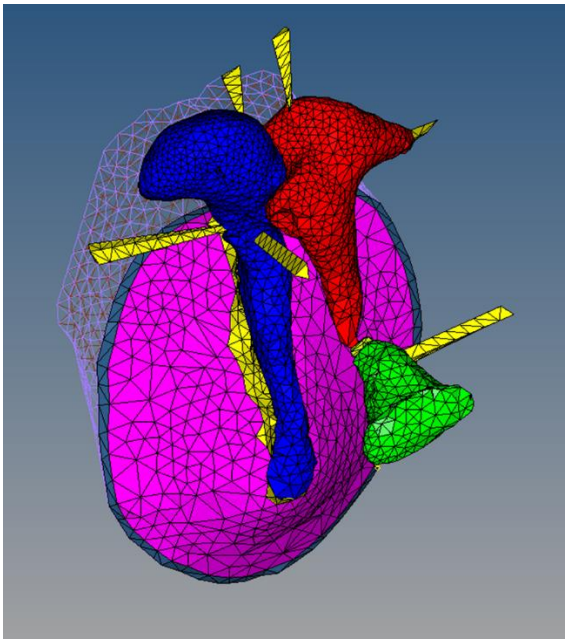

Figure 14. Newborn baboon ear structures shown with suspensory ligaments as boundary conditions.

The middle ear geometries discussed in this topic do not include the cochlear structure. To account for the effects of the presence of the cochlea in a healthy baboon, a cochlear load is applied at the stapes footplate. As the human FE model became more accurate, the cochlear load was modeled as a dashpot system that creates a damping effect on the footplate's movement. Figure 15 demonstrates how this was modeled in ANSYS Mechanical.

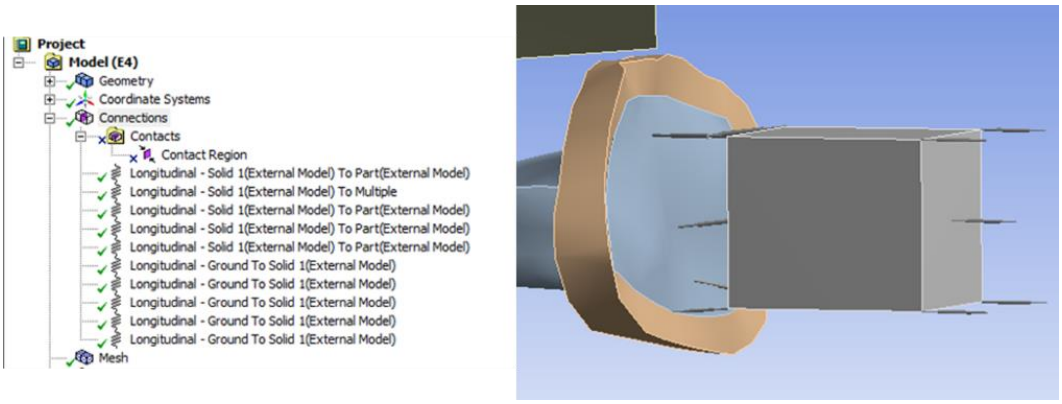

Figure 15. Example of modeling cochlear load as a dashpot system in ANSYS Mechanical.

A cube representing cochlear mass was placed normal to the stapes footplate, which it was attached to by five one-dimensional spring dashpots. On the other side of the cochlear mass were 5 more springs which connecting the mass and ground. Three degrees of freedom exist at each node: translation in the x, y, and z directions. Furthermore, the elements exhibit viscoelasticity, large deflection, and large strain capabilities. Because no data exists for the baboon cochlear load, the human cochlear load was selected [33]. The cochlear load dashpot damping system modeled a 20 GΩ acoustic impedance, the ratio of acoustic pressure to acoustic volume flow, applied to the stapes footplate [21].

2.2.3 Material and Mechanical Properties

As discussed in the Introduction of this thesis, no publications discuss the mechanical properties of the baboon middle ear structures, so other species must be investigated. The most complete publications of mechanical properties for middle ear structures are of the chinchilla and human. Of these, the human is the obvious choice for a model prototype because of species similarities, particularly

in general shape of the skull and closer genetic correlation [11]. For the analyses discussed here, the mechanical properties of the baboon model were assigned based on the published properties of the pediatric and adult human ear tissues listed in Table 1.

From a mechanical engineering perspective, many materials are described as having either viscous or elastic properties. Many biomaterials, however, are considered viscoelastic in nature, meaning they have both viscous and elastic behavior [18,34]. To describe the viscoelastic behavior of the soft tissues of the middle ear, the generalized linear solid model was employed in this study. Based on this model, the relaxation modulus is described as:

$$E(t) = E_0 + \sum_{i=1}^{n} E_i \exp\left(-\frac{t}{\tau_i}\right)$$

where E_i (i=0,1,…., n) is the relaxation modulus of the *i* th spring, τ_i is the relaxation time of the *i* th dashpot. For harmonic analysis, $E(t)$ in the time domain can be converted into the complex modulus in the frequency domain as

$$E^*(f) = E'(f) + iE''(f)$$

where $E'(f)$ is the storage modulus, $E''(f)$ is the loss modulus, f is the frequency, and $E'(f)$ and $E''(f)$ can be expressed as:

$$E'(f) = E_0 + \sum_{i=1}^{n} E_i \tau_i^2 \left(\frac{2\pi f^2}{1 + \tau_i^2 (2\pi f)^2}\right)$$

$$E''(f) = \sum_{i=1}^{n} E_i \tau_i \left(\frac{2\pi f}{1 + \tau_i^2 (2\pi f)^2} \right)$$

$$\eta(f) = \tan \delta = \frac{E''(f)}{E'(f)}$$

where δ is the phase angle of the complex modulus, and η(*f*) is the loss factor defined as the ratio of the storage modulus to the loss modulus.

Viscoelastic material properties were assigned to the middle ear soft tissues including the TM pars flaccida, TM pars tensa, incudomallear joint, incudostapedial joint, stapedial annular ligament, and round widow membrane. As demonstrated above, the relaxation modulus of each of these tissues was be expressed by using standard solid model formulae and were easily converted into a frequency-dependent complex modulus, which was input into the FE model before sound transmission analysis. After setting n=1 as done previously, the final viscoelastic defining equation is

$$E(t) = E_0 + E_1 \exp\left(-\frac{t}{\tau_1}\right)$$

where E_1 is the relaxation modulus of the spring and τ_1 is the relaxation time of the dashpot. These material parameters, E_0, E_1, and τ_1 were obtained from a previous study performed in our research group involving dynamic material tests

and the cross-calibration method and are listed in Table 1. Other components of the ear canal and middle ear used the same material properties as our previous FE model [21,35].

Table 1. Mechanical properties used for finite element analysis, based on human values from previous studies [Gan and Zhang, 2011].

Structure	Newborn	Adult
Tympanic membrane		
Para tensa		
E0 (MPa)	20	25
E1 (MPa)	15	70
τ1 (μs)	25	25
Pars flaccida		
E0 (MPa)	7	7
E1 (MPa)	16	16
τ1 (μs)	25	25
Manubrium		
Elastic modulus (MPa)	4700	4700
Incudomalleolar joint		
E0 (MPa)	60	60
E1 (MPa)	180	180
τ1 (μs)	20	20
Inducostapedial joint (ISJ)		
E0 (MPa)	2.5	0.4
E1 (MPa)	10	20
τ1 (μs)	20	20
Stapedial annular ligament (SAL)		
E0 (MPa)	2.5	2
E1 (MPa)	10	10.8
τ1 (μs)	20	20
Superior mallear ligament (C1)		
Elastic modulus (MPa)	4.9	4.9
Lateral mallear ligament (C2)		
Elastic modulus (MPa)	6.7	6.7
Posterior incudal ligament (C3)		
Elastic modulus (MPa)	6.5	6.5
Anterior mallear ligament (C4)		
Elastic modulus (MPa)	8	8
Posterior stapedial tendon (C5)		
Elastic modulus (MPa)	10	10
Tensor tympani tendon (C7)		
Elastic modulus (MPa)	8	8
Round window membrane (RWM)		
E0 (MPa)	1	1
E1 (MPa)	3	3
τ1 (μs)	30	30

2.3 Model Validation

In order to assess the integrity of the FE models, model validation was performed. For the newborn finite element model, a group of N=6 baboon temporal bones ranging in age from 0 days to 1.5 years in age. This age group is analogous to a human age group of newborn to approximately 4.5 years in age, making it comparable to a pediatric human model. To assess the adult model, a group of N=6 baboon temporal bones ranging from 6 years to 11 years old were measured for comparison with the analysis results. This age group is analogous to a human age group of approximately 18 years to 33 years in age, making it comparable to an adult human model. Both groups included the actual temporal bones used to build the 3D models discussed here.

In each temporal bone, TM vibration at the umbo, the lowest point of contact with the malleus at the center of the membrane (Figure 16), was measured using laser Doppler vibrometry (LDV). The performance of these LDV experiments was monitored by Don Nakmali in Stephenson Technology and Research Center at the University of Oklahoma. A sound delivery tube and a probe microphone were placed in the ear canal to measure the movement of the TM at this location. The laser beam from the LDV is directed at the surface of interest, in this case the umbo of the TM, and the vibration amplitude and frequency are extracted from the Doppler shift of the reflected laser beam frequency due to the motion of the surface.

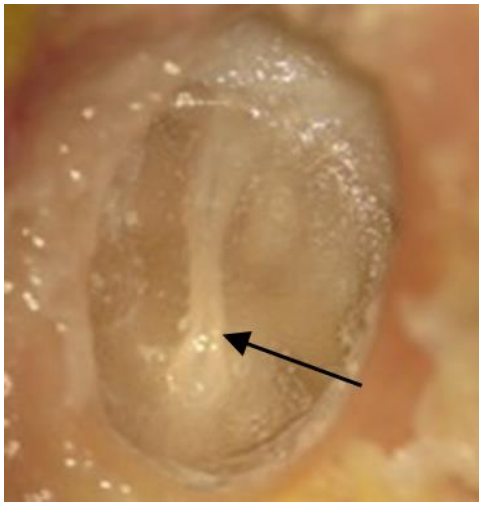

Figure 16. Lateral view of tympanic membrane of baboon with umbo indicated.

The methods of stimulus generation and umbo vibration measurement closely resembled those previously published by Guan et al. [36]. Briefly, pure tones at 90 dB sound pressure level (SPL) were presented into the ear canal sequentially from 100 Hz to 10 kHz for 50 cycles at each tone via a sound delivery tube. As shown in Figure 17, a probe microphone (Model ER-7C, Etymotic Research, IL) was inserted in the ear canal and the tip of the probe was placed approximately 2 mm from the umbo to monitor the input SPL. After the sound delivery tube and the probe microphone were placed, the entrance of the ear canal was sealed with dental cement.

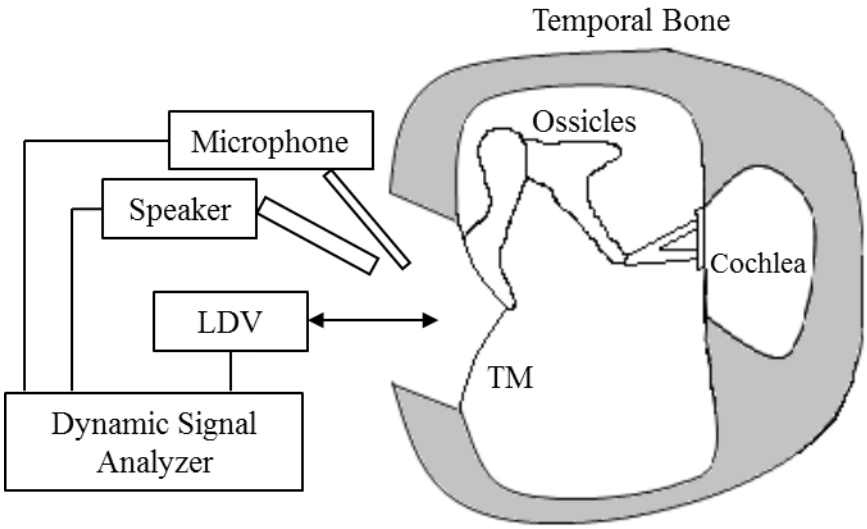

Figure 17. Laser Doppler vibrometry setup for performance in a baboon ear.

The opening in the lateral surface of the baboon ear canal wall was covered by a transparent glass sheet, and the gap between the glass sheet and the bony wall was also sealed with dental cement. Vibrations of the TM were measured by the laser vibrometer (Polytec CLV 2534, Tustin, CA). The direction of the laser beam was approximately normal to the lateral surface of the umbo. The peak-to-peak displacements ($d_{p\text{-}p}$ in unit of μm) of the TM at the umbo were calculated from the voltage output of the laser vibrometer velocity decoder by

$$d_{p-p} = \frac{2A_{volt}}{\pi f}$$

where A_{volt} is the amplitude of vibrometer output (velocity) in Volts and f is the frequency of pure tone in kHz.

One sample was measured at 80 dB instead of 90 dB. Because there is a direct relationship between voltage and pressure, both values were converted from decibels to Pascals, and the ratio between them was multiplied by the voltage values before converting to micrometers. This step later proved to be unnecessary when each displacement value was divided by the pressure to obtain units in displacement in micrometers per Pascal. This unit controls for the sound pressure selected by other research groups, allowing the data to be more comparable to other existing publications using LDV to measure umbo displacement. The LDV data collected will be compared to the finite element model's measurement of the umbo displacement for validation purposes.

Chapter 3: Newborn Baboon Ear Findings

3.1 Newborn 3D Model

While 1260 tomographic images were taken of the newborn ear, only 1138 were used to create the geometry of the middle ear and the middle ear cavity. As shown in Table 2, the newborn TM was 4.53 mm along the major axis of the elliptical shape and 4.44 mm along the minor axis. It was modeled approximately 40 μm thick, and had a surface area of 19.44 mm^2. The newborn TM had a conic depth of 3.12 mm and sat at an angle of approximately 78º from horizontal, with the superior leaning further out toward the ear canal. The malleus is 3.43 mm in length, with the head being 1.57 mm at the widest point and the neck being 0.47 mm across on average.

Table 2. Newborn baboon middle ear dimensions where the elliptical TM is described using the major and minor axis terminology.

Structure	Newborn
Tympanic Membrane	
Major axis (mm)	4.53
Minor axis (mm)	4.44
Conic depth (mm)	3.12
Thickness (μm)	40
Surface Area (mm^2)	19.44
Angle from Horiz. (°)	77.60
Malleus	
Length (mm)	3.43
Width, head (mm)	1.57
Width, neck (mm)	0.47
Incus	
Length (mm)	2.21
Width, head (mm)	1.65
Width, neck (mm)	0.40
Stapes	
Height (mm)	1.54
Width (mm)	0.95
Angle from Horiz. (°)	25.50
Ear Canal Opening	
Height (mm)	4.18
Width (mm)	2.16
Middle Ear Cavity	
Height (mm)	7.73
Width (mm)	7.98

The newborn incus measured 2.21mm in length and the head had a width of 1.65mm while the neck had a width of 0.40 mm on average. Next, the stapes was 1.54 mm in height and the footplate was 0.95 mm lengthwise. The stapes sits

at an approximately 25 º angle from horizontal, and as shown in Figure 18, points at a slight downward angle from where it attaches to the incus.

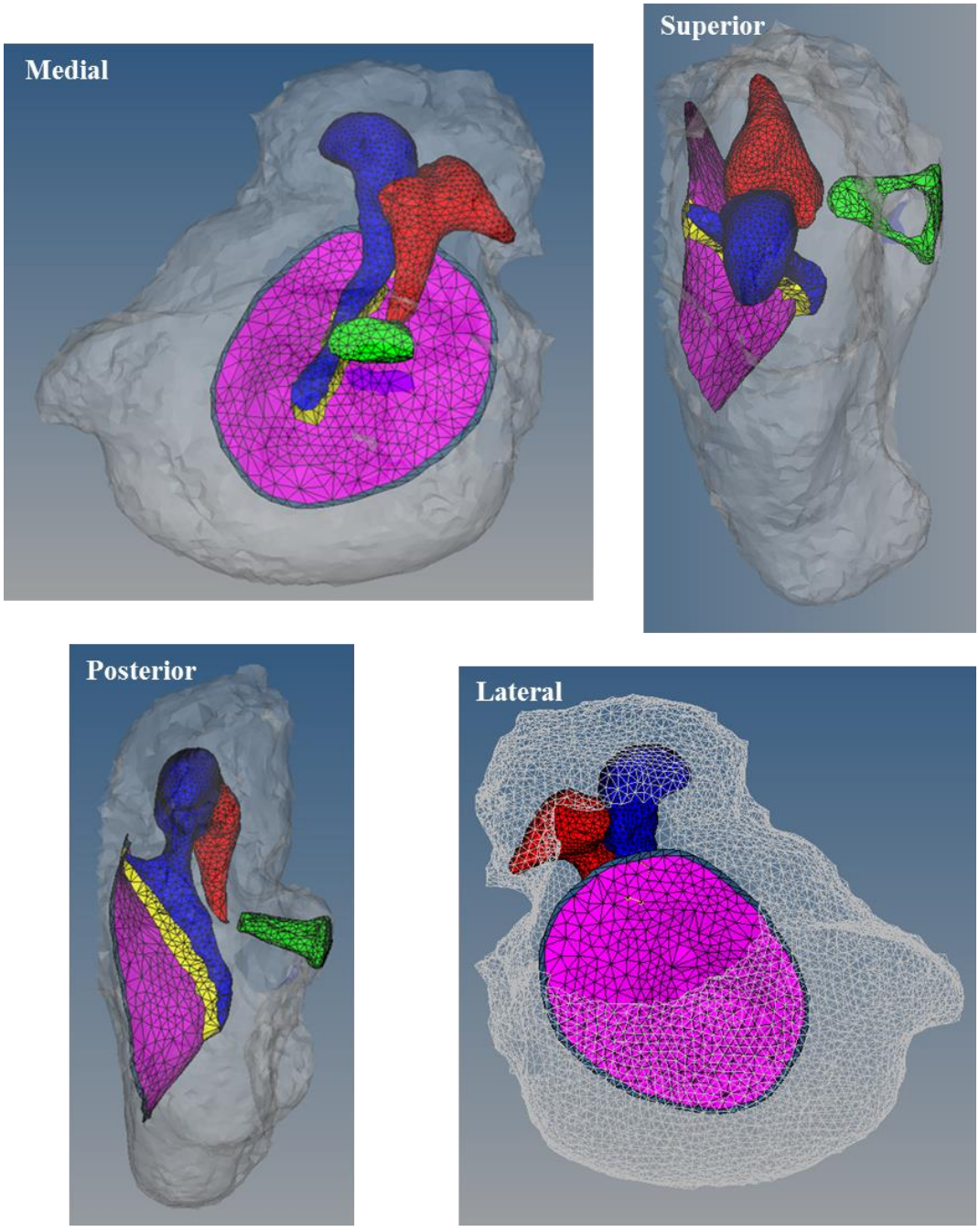

Figure 18. Finite element mesh of newborn male baboon middle ear cavity, ossicles, and tympanic membrane from medial, superior, posterior, and lateral views.

The newborn ear canal opening is 4.18 mm in height and 2.16 mm in width, making it slightly smaller than the TM in height, but considerably less wide. The middle ear cavity is 7.73 mm in height and 7.98 mm in width, making it nearly twice as tall and wide as the TM.

Table 3. Final element count for newborn baboon finite element model.

Newborn	Nodes	Elements
TM	808	1502
Stapes	456	2167
Malleus	1965	7465
Incus	1106	4137
Annulus	224	224
ME Cavity (surface)	5488	10851

Table 3 depicts the total number of elements in each key component. The TM consisted of 1502 flat 3D elements with 808 nodes. The stapes consisted of 2167 3D elements with 456 nodes. The malleus consisted of 7465 3D elements and 1965 nodes. The incus consisted of 4137 3D elements and 1106 nodes. The annulus was comprised of 224 flat 3D elements and 224 nodes. Unsurprisingly, the middle ear cavity surface was the most complex as it was comprised of 10851 two-dimensional elements with 5488 nodes. As is visible in Figure 19, the ossicles all had similarly sized elements, while the middle ear cavity, inlet, and ear canal all had slightly larger elements due to their simplicity and larger size.

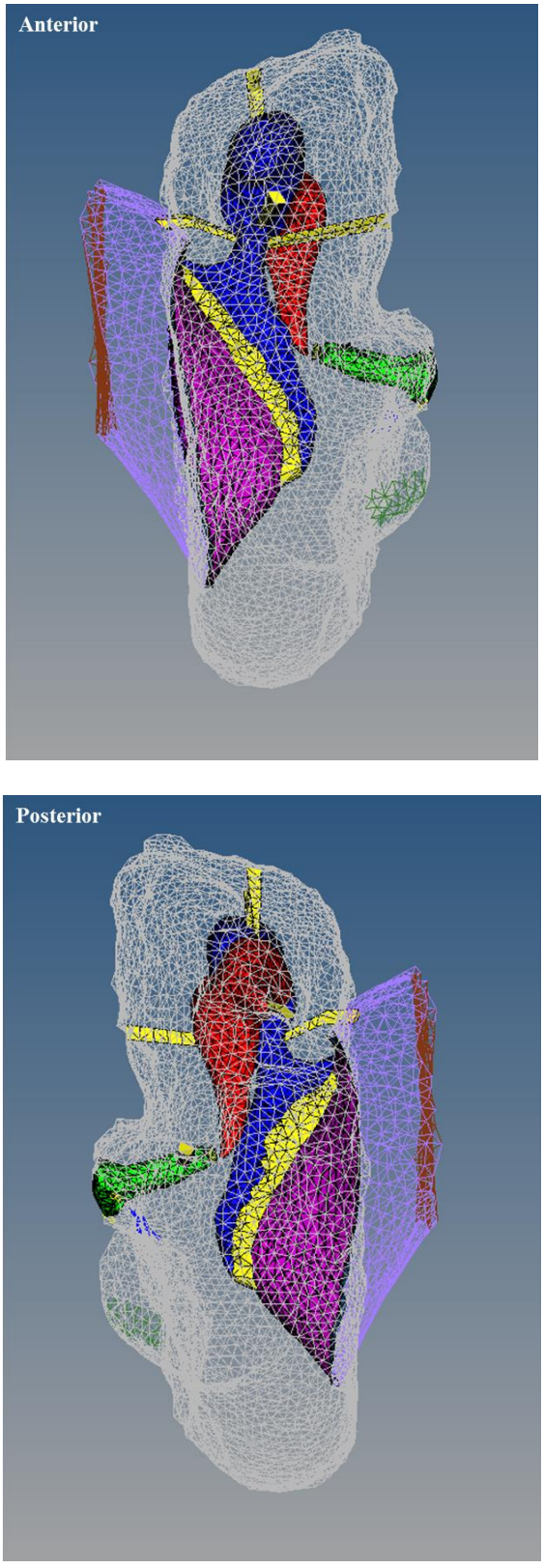

Figure 19. Anterior and posterior view of the newborn middle ear model, complete with ear canal.

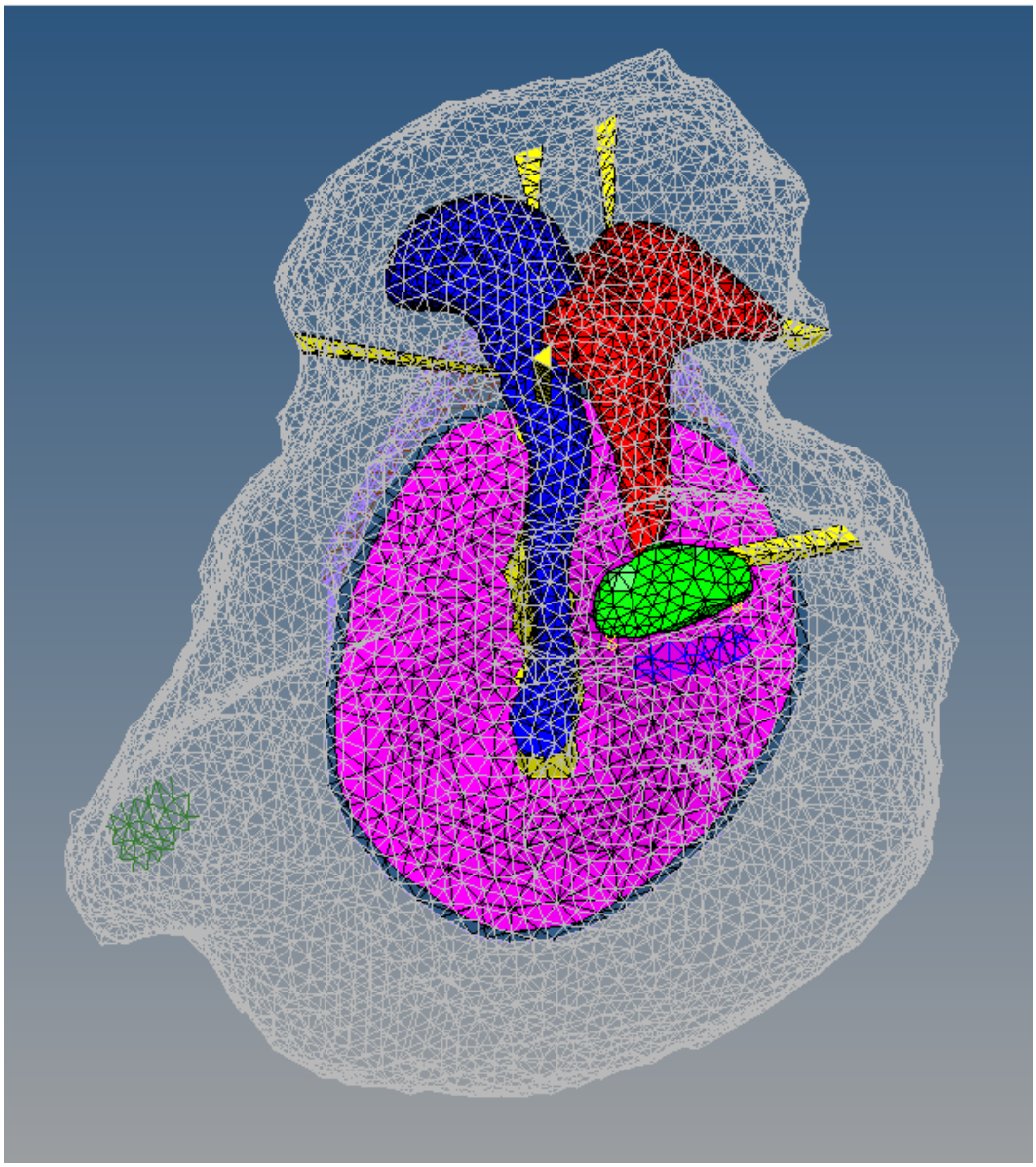

Figure 20. Enlarged medial view of complete newborn middle ear model.

In Figure 20, the green Eustachian tube opening for the newborn baboon is visible to the left of the image. Beneath the stapes footplate is the round window membrane in royal blue. Both were modeled based on dissection observations and micro-CT scans.

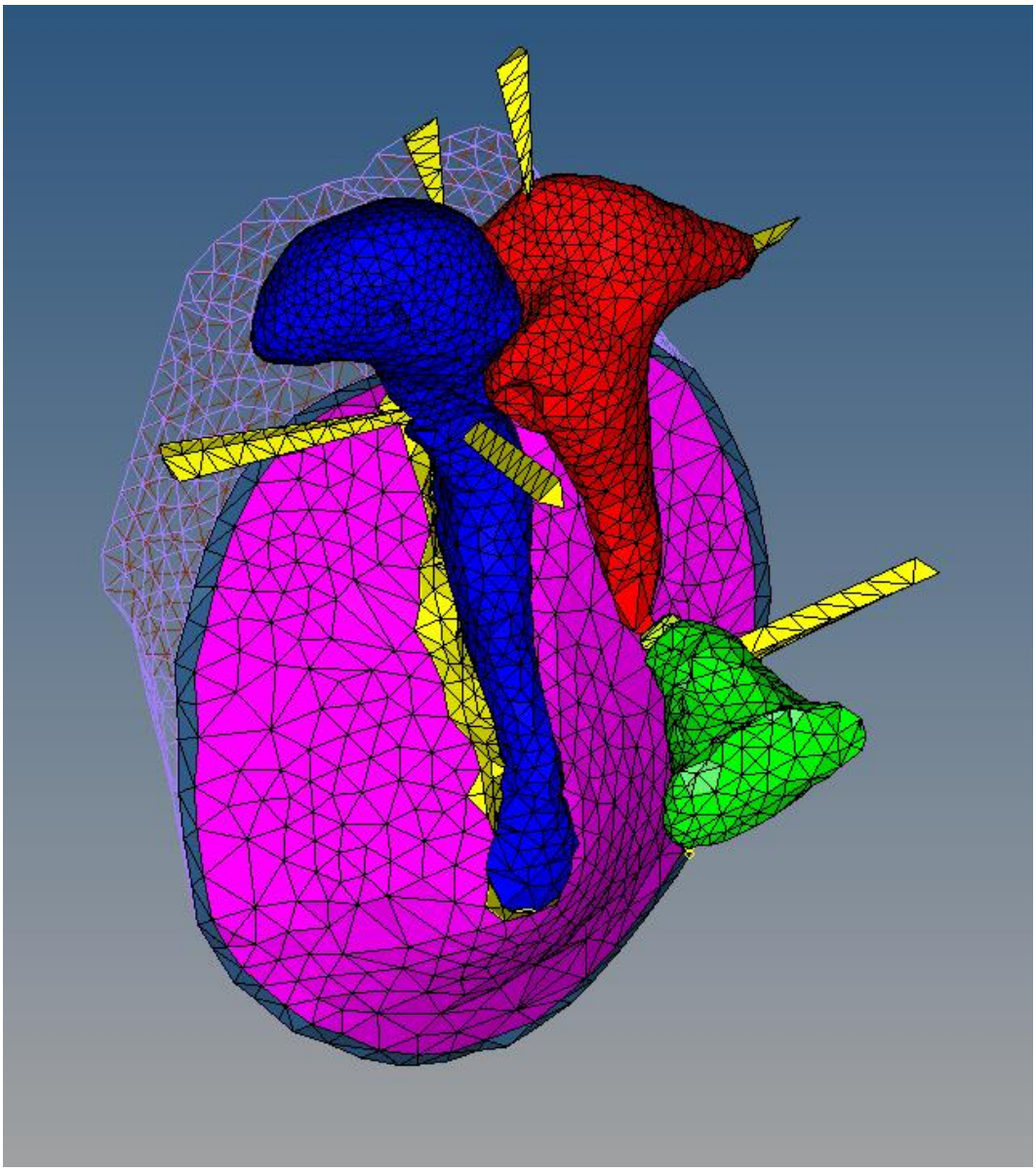

Figure 21. Enlarged medial-superior view of the newborn middle ear displaying ligaments and ear canal.

In Figure 21, the triangular and tetrahedral shapes of the elements of the newborn baboon model can be clearly observed. The malleus, shown in blue, tucks neatly into the incus, shown in red, to create the incudomalleolar joint. A medial view of the ear canal is also visible.

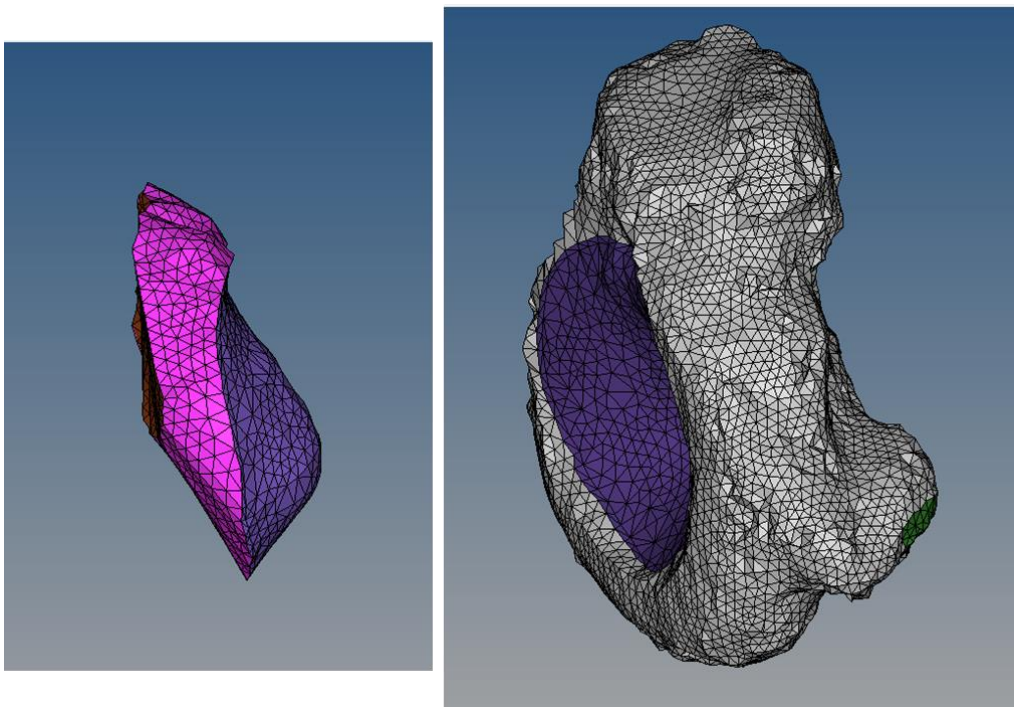

Figure 22. Newborn fluid domains, with the ear canal domain on the left and the middle ear domain on the right.

After preparation for fluid analysis, ear canal and middle ear cavity fluid domains were clearly defined. After the modeling described in Methods, the newborn ear was left the fluid domains depicted in Figure 22. The brown inlet, pink ear canal, and purple TM FSIs are shown on the left, while the purple TM, grey MEC, and green Eustachian tube FSIs are shown on the right. The RWM and SAL FSIs are present in the middle ear cavity fluid domain but are not visible in Figure 22.

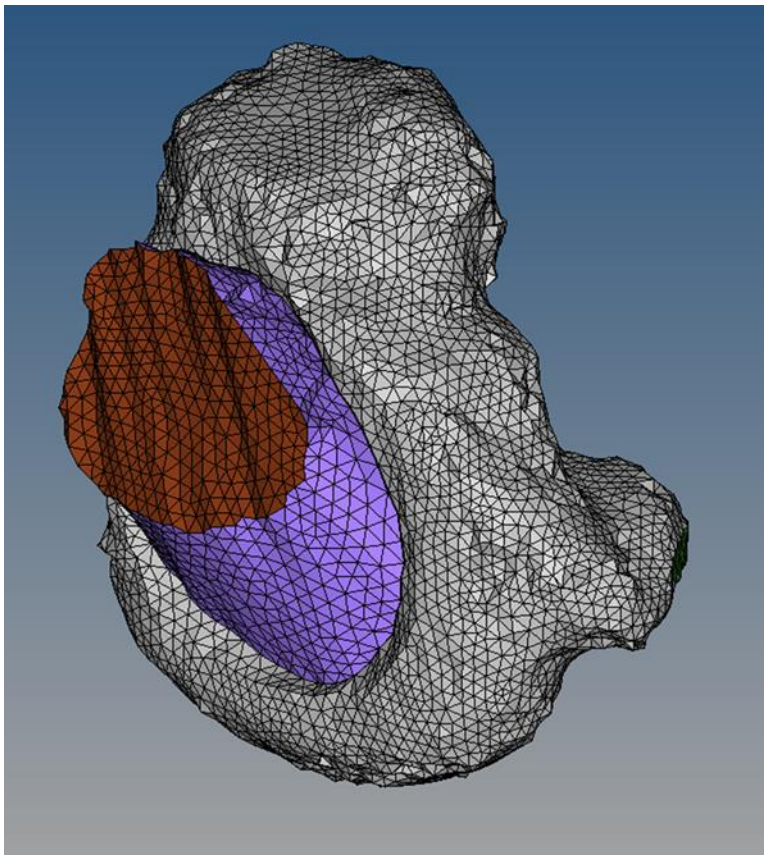

Figure 23. The newborn fluid domains in the context of each other.

The above Figure 23 demonstrates how the ear canal was modeled to connect directly to the TM, while the middle ear cavity encompasses and curves around the TM. The brown inlet is clearly visible at the opening of the ear canal. Sound transmission was modeled as coming from the inlet. The two fluid domains sandwich the TM and annulus.

3.2 Newborn Analysis of Sound Transmission

After analysis was run, the results needed to be compared to experimental data to determine the integrity of the model. To do this, six baboon temporal bones each less than 1.5 years old (correlating with human age 0 to ~ 4.5 years),

were experimentally tested using LDV. The group consisted of 4 female and 2 male bones, including the male newborn temporal bone on which the FE model is based.

The results are plotted on Figure 24 with umbo peak to peak displacement on the y axis and frequency in Hz on the x-axis. Each sample's individual experimental data is shown in grey, while the experimental mean is shown in a black dotted line and the thick blue line is the output from the newborn baboon FE model assigned with human pediatric mechanical properties from Table 1 and the cochlear load of 20 GΩ impedance.

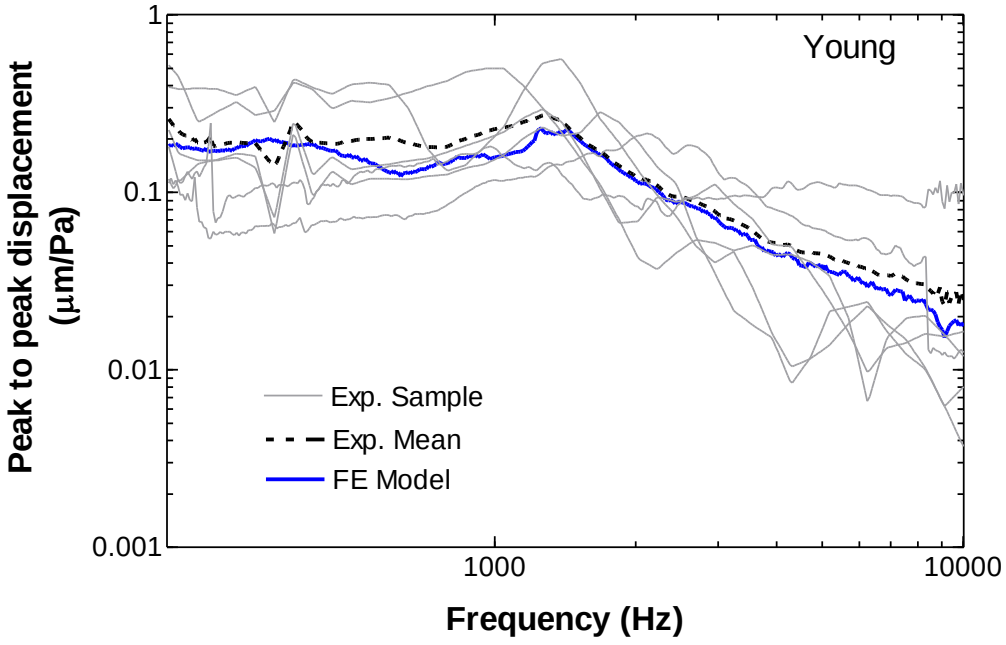

Figure 24. Newborn baboon experimental (N=6) and finite element model results for TM displacement at the umbo across a frequency range.

The frequency range is displayed from 200-10000 Hz, and the umbo displacement varied from 0.05 to 0.50 μm/Pa at the lower frequencies while it

varied from 0.004 to 0.14 μm/Pa at higher frequencies. The mean was approximately 0.23 μm/Pa at 200 Hz, 0.24 μm/Pa at 1200 Hz, and 0.025 μm/Pa at 10000 Hz. Similarly, the FE model had a displacement of 0.18 μm/Pa at 200 Hz, 0.21 μm/Pa at 1200 Hz, and 0.019 μm/Pa at 10000 Hz. Treating the experimental mean as the accepted value and the FE results as the those to be compared, this gives a percent error of 21.7% at 200 Hz, 12.5% at 1200 Hz, and 24% at 10000 Hz. Overall, the experimental mean and FE model seem to exhibit the most similar TM umbo movement at moderate frequency levels, 1100-3500 Hz.

Chapter 4: Adult Baboon Ear Findings

4.1 Adult 3D Model

Like with the newborn, not all the slides were used for 3D reconstruction. While 1315 tomographic images were taken of the adult ear, only 1207 were used to create the geometry of the middle ear and the middle ear cavity. As shown in Table 4, the adult TM was 5.30 mm along the major axis and 4.05 mm along the minor axis. It was modeled approximately 0.25 mm thick, and had a surface area of 20.73 mm^2. The adult TM had a conic depth of 2.56 mm and sat at an angle of approximately 46º from horizontal, with the superior leaning further out toward the ear canal. The malleus is 3.22 mm in length, with the head being 1.94 mm at the widest point and the neck being 0.49 mm across on average.

The adult incus measured 2.60 mm in length and the head had a width of 1.56mm while the neck had a width of 1.34 mm on average. Next, the stapes was 1.85 mm in height and the footplate was 0.95 mm lengthwise. The stapes sits at

an approximately 40 º angle from horizontal, and as shown in Figure 24, points straight out, if not at a slightly upward angle from where it attaches to the incus.

Table 4. Adult baboon middle ear dimensions where the elliptical TM is described using the major and minor axis terminology.

Structure	Adult
Tympanic Membrane	
Major axis (mm)	5.30
Minor axis (mm)	4.05
Conic depth (mm)	2.56
Thickness (μm)	25
Surface Area (mm^2)	20.73
Angle from Horiz. (°)	46.30
Malleus	
Length (mm)	3.22
Width, head (mm)	1.94
Width, neck (mm)	0.49
Incus	
Length (mm)	2.60
Width, head (mm)	1.56
Width, neck (mm)	0.38
Stapes	
Height (mm)	1.85
Width (mm)	1.34
Angle from Horiz. (°)	39.90
Ear Canal Opening	
Height (mm)	5.02
Width (mm)	2.54
Middle Ear Cavity	
Height (mm)	9.29
Width (mm)	5.19

The adult ear canal opening is 5.02 mm in height and 2.54 mm in width, again making it slightly smaller than the TM in height, but considerably less wide. The middle ear cavity is 9.29 mm in height and 5.19 mm in width, making it nearly twice as tall as but only a small amount wider than the TM.

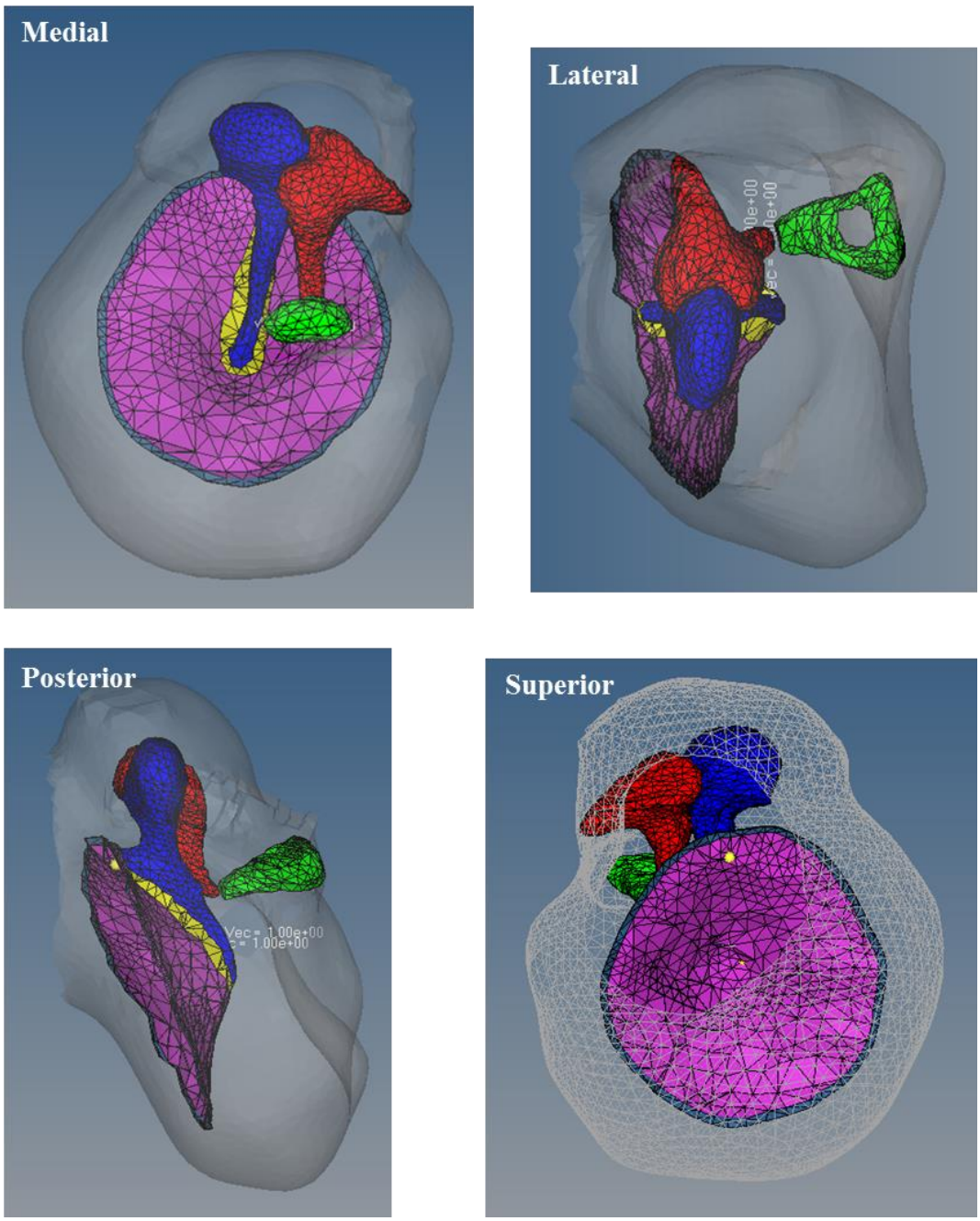

Figure 25. Finite element mesh of female adult baboon middle ear cavity, ossicles, and tympanic membrane from medial, superior, posterior, and lateral views.

Table 5 depicts the total number of elements in each key component of the adult baboon FE model. The TM consisted of 1354 flat 3D elements with 750 nodes. The stapes consisted of 2021 3D elements with 410 nodes. The malleus

consisted of 5442 3D elements and 1080 nodes. The incus consisted of 4935 3D elements and 1175 nodes. The annulus was comprised of 314 flat 3D elements and 314 nodes.

Table 5. Final element count for adult baboon finite element model.

Adult	Nodes	Elements
TM	750	1354
Stapes	410	2021
Malleus	1080	5442
Incus	1175	4935
Annulus	314	314
ME Cavity (surface)	5506	10948

The middle ear cavity surface had both the most elements and the most nodes as it was comprised of 10948 two-dimensional elements with 5506 nodes. As is visible in Figure 26, the ossicles all had similarly sized elements, while the middle ear cavity, inlet, and ear canal all had slightly larger elements due to their simplicity and the larger size of the structures.

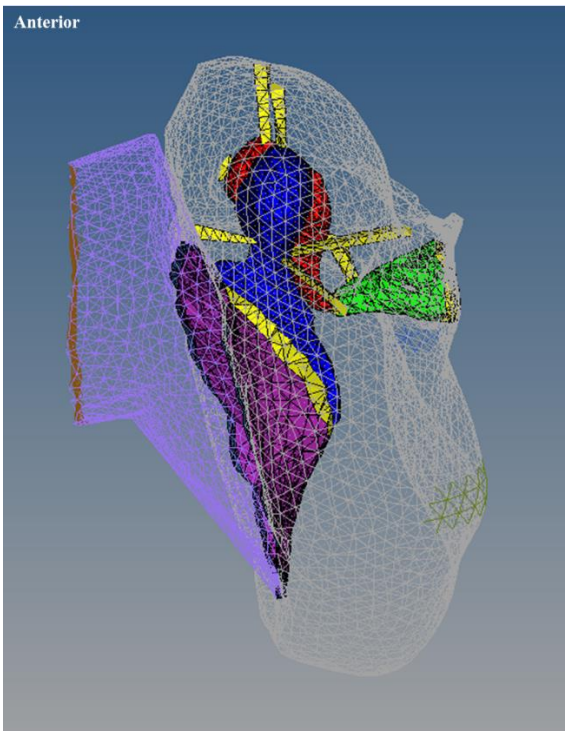

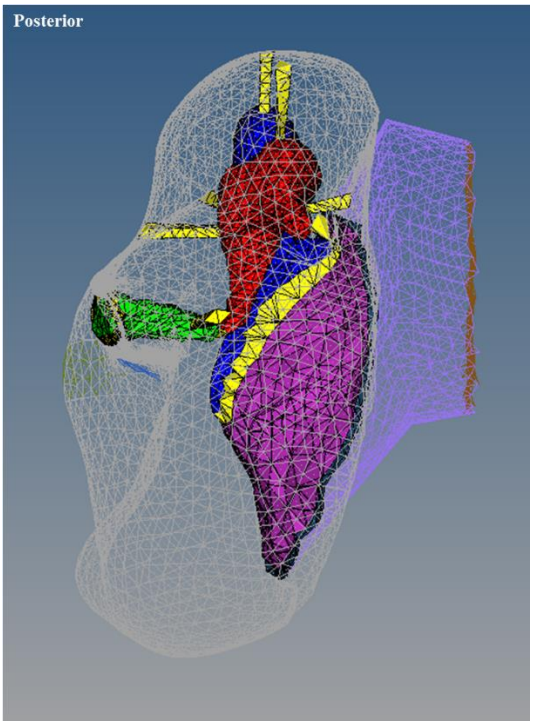

Figure 26. Anterior and posterior view of the adult middle ear model, complete with ear canal.

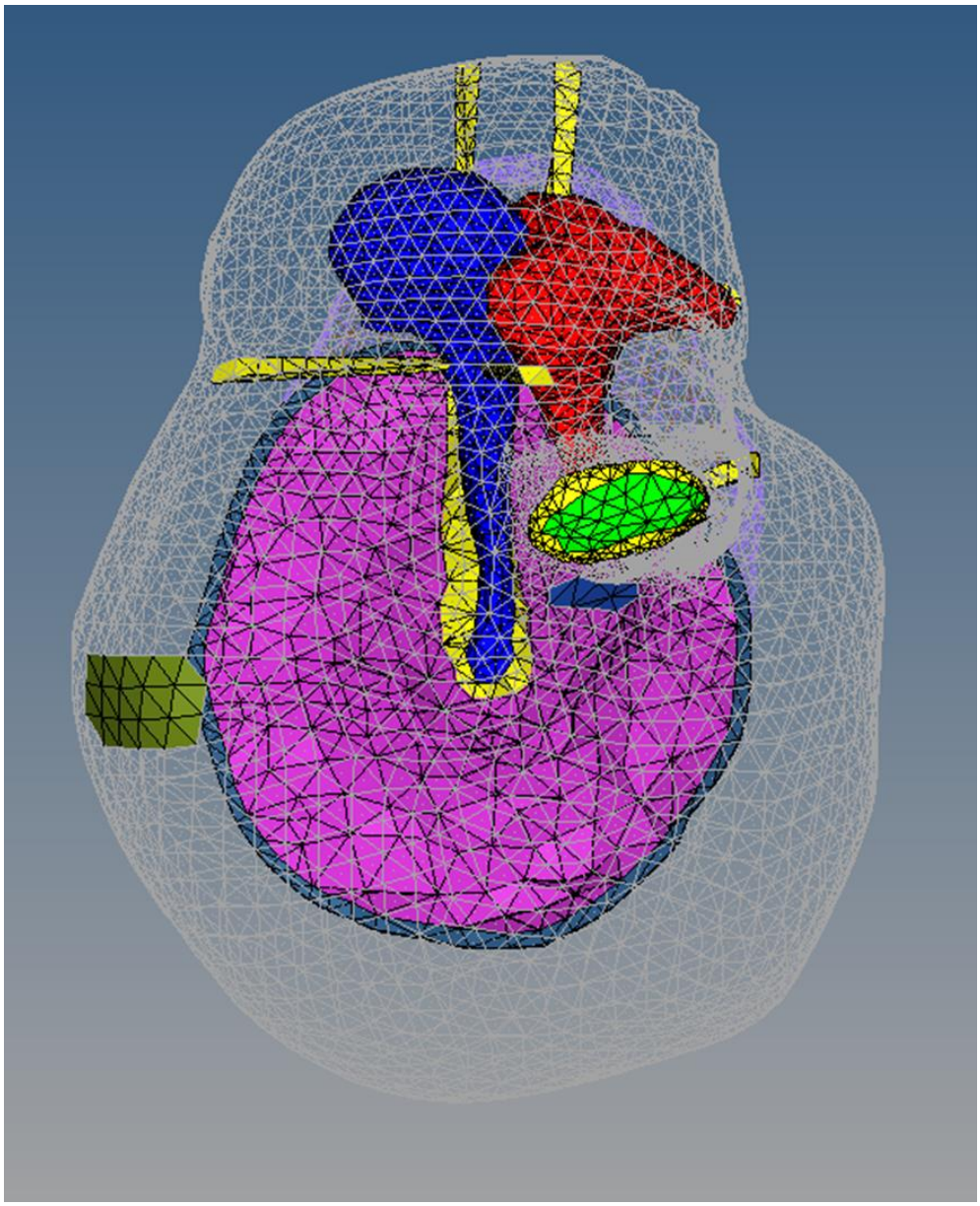

Figure 27. Enlarged medial view of complete adult middle ear model.

In Figure 27, the green Eustachian tube opening for the adult baboon is visible in the left of the image. Beneath the stapes footplate is the round window membrane in royal blue. Both were modeled based on surgical dissection observations and micro-CT scans.

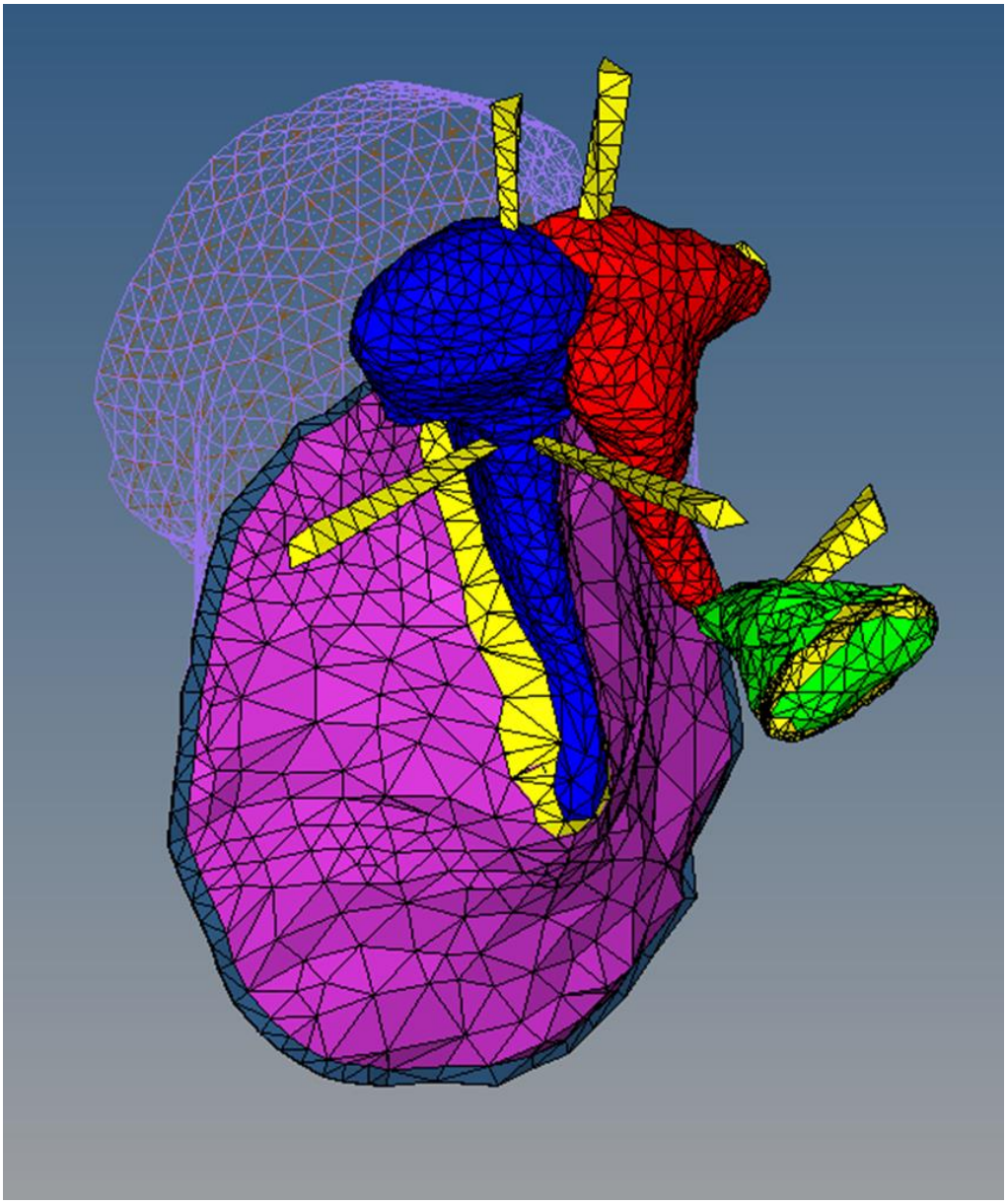

Figure 28. Enlarged medial-superior view of the adult middle ear displaying ligaments and ear canal.

In Figure 28, the triangular and tetrahedral shapes of the elements in the adult model can be clearly observed. The malleus head, shown in blue, tucks neatly into the incus, shown in red, to create the incudomalleolar joint. A medial view of the adult ear canal is also visible.

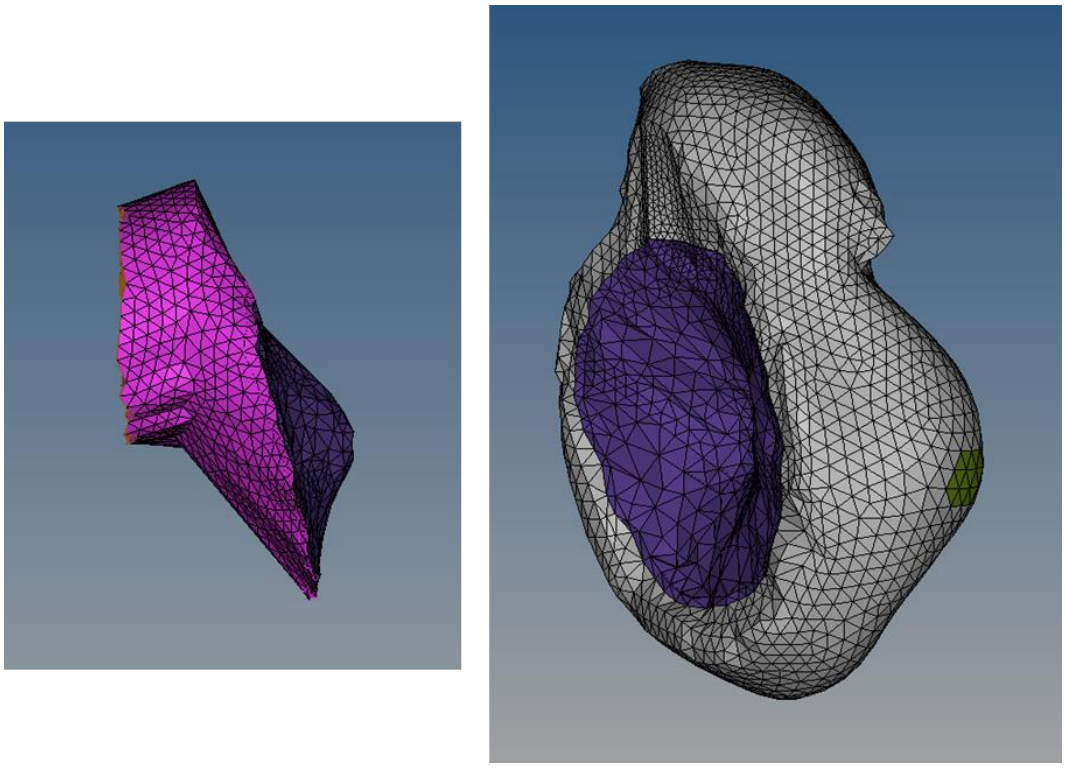

Figure 29. Adult fluid domains, with the ear canal domain on the left and the middle ear domain on the right.

After preparation for fluid analysis, the ear canal and middle ear cavity fluid domains were clearly defined. After the mesh manipulation discussed previously, the adult ear was left the fluid domains depicted in Figure 29. The brown inlet, pink ear canal, and purple TM FSIs are shown on the left, while the purple TM, grey MEC, and green Eustachian tube FSIs are visible on the right. The RWM and SAL FSIs are present in the middle ear cavity fluid domain but are not visible in Figure 29.

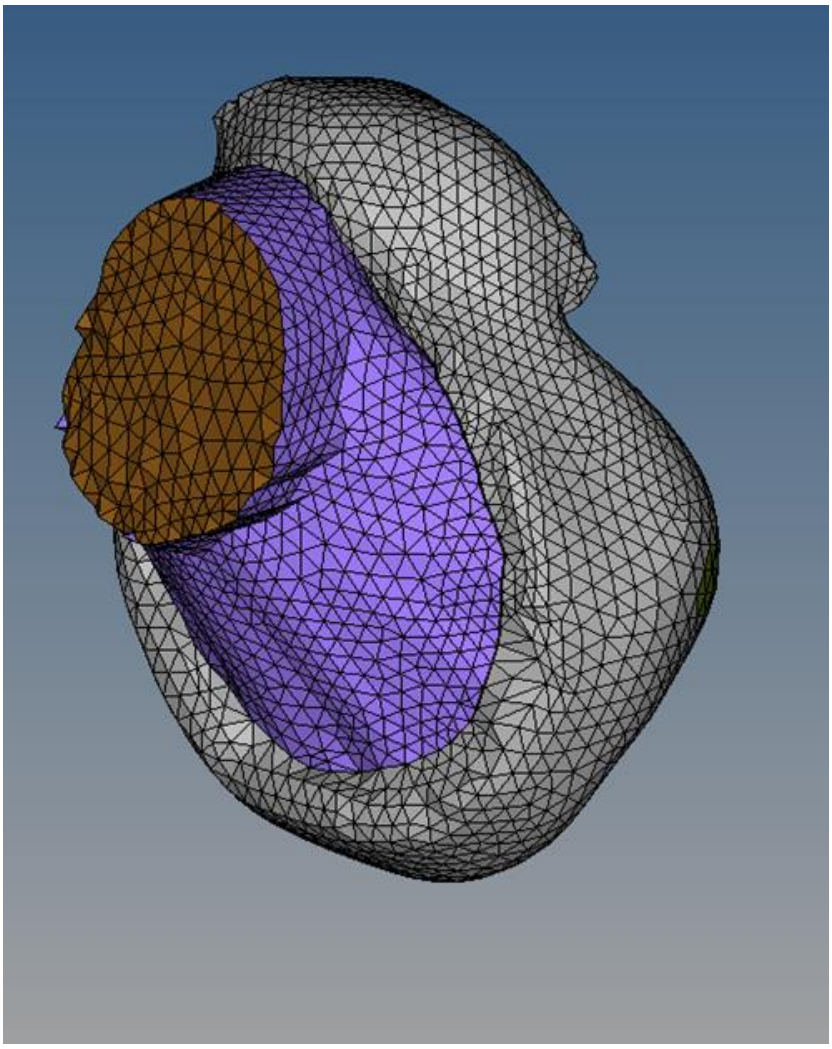

Figure 30. The adult fluid domains in the context of each other.

Above, Figure 30 demonstrates how the ear canal was modeled to connect directly to the TM while the middle ear cavity encompasses and curves around the TM a bit more. The brown inlet is clearly visible at the opening of the ear canal. Sound transmission was modeled as coming from the inlet FSI. The two fluid domains sandwich the TM and annulus.

4.2 Adult Analysis of Sound Transmission

After analysis was run, the results were compared to experimental data to determine the integrity of the model. To do this, six baboon temporal bones ranging from 6 to 11 years old (correlating approximately with human age ~18-33 years), were experimentally tested using LDV. Like the newborn experimental group, the adult experimental group consisted of 4 female and 2 male bones, including the female 11 year old temporal bone on which the FE model is based.

The results are plotted on Figure 31 with umbo peak to peak displacement on the y axis and frequency in Hz on the x-axis. Each sample's individual experimental data is shown in grey, while the experimental mean is shown in a black dotted line and the thick blue line is the output from the adult baboon FE model assigned with human adult mechanical properties from Table 1 and the cochlear load of 20 GΩ impedance.

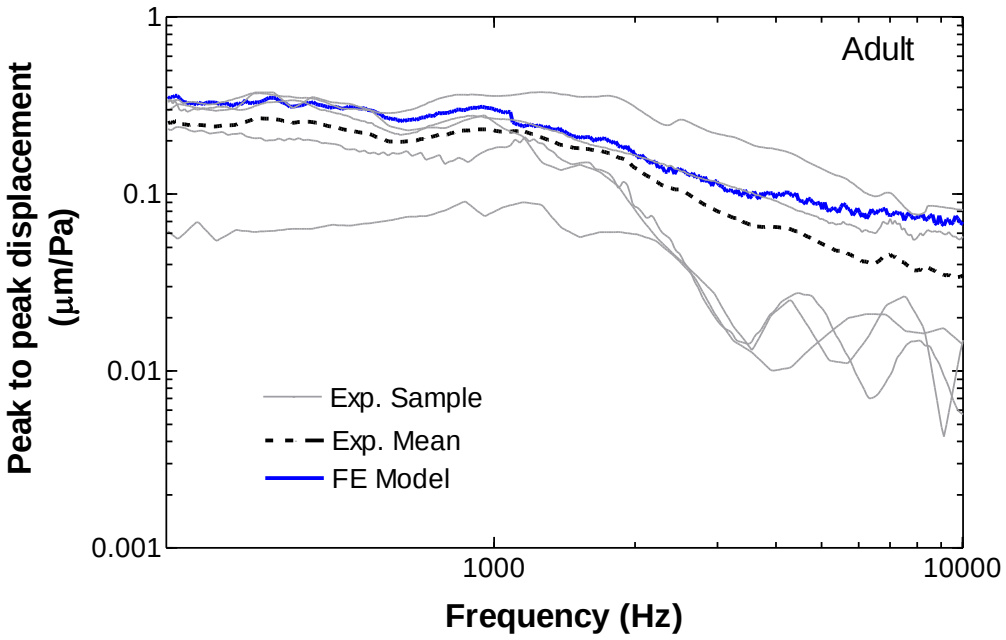

Figure 31. Newborn baboon experimental (N=6) and finite element model results for TM displacement at the umbo across a frequency range.

The frequency range is displayed from 200-10000 Hz, and the umbo displacement for adult baboons varied from 0.06 to 0.32 µm/Pa at the lower frequencies while it varied from 0.004 to 0.08 µm/Pa at higher frequencies. The mean was approximately 0.26 µm/Pa at 200 Hz, 0.21 µm/Pa at 1200 Hz, and 0.036 µm/Pa at 10000 Hz. Similarly, the FE Model had a displacement of 0.34 µm/Pa at 200 Hz, 0.27 µm/Pa at 1200 Hz, and 0.074 µm/Pa at 10000 Hz. Treating the experimental mean as the accepted value and the FE results as the results to be compared, this gives a percent error of 30.7% at 200 Hz, 28.5% at 1200 Hz, and 105% at 10000 Hz. Displacement values at very high frequencies deviate significantly, but overall the shape of the FE curve is similar to that of the experimental curve.

Chapter 5: Discussion

5.1 Middle Ear Structures

Overall, the newborn and adult baboon ears were fairly similar in size and shape, but there were several differences. As would be expected, most structures were slightly larger in the adult if not the same as the newborn in size. As shown in Table 6, the adult TM had more height (major axis) but less width (minor axis) than the newborn. It was also oriented differently inside the middle ear cavity, and was lower with respect to the ear canal. The adult malleus is slightly shorter than that of the newborn, but is wider at the head and similar in width at the neck. Next, the adult incus is longer than that of the newborn, while the width of the head and neck are slightly smaller and about the same, respectively. The adult stapes is both longer and wider than the newborn stapes and is also oriented differently inside the middle ear cavity. While the adult stapes appears to point straight out and slightly upward with respect to the other structures, the newborn stapes sits at a slightly downward angle.

Table 6. A comparison between adult and newborn baboon ear dimensions.

Structure	Adult	Newborn
Tympanic Membrane		
Major axis (mm)	5.30	4.53
Minor axis (mm)	4.05	4.44
Conic depth (mm)	2.56	3.12
Thickness (μm)	25	40
Surface Area (mm^2)	20.73	19.44
Angle from Horiz. (°)	46.30	77.60
Malleus		
Length (mm)	3.22	3.43
Width, head (mm)	1.94	1.57
Width, neck (mm)	0.49	0.47
Incus		
Length (mm)	2.60	2.21
Width, head (mm)	1.56	1.65
Width, neck (mm)	0.38	0.40
Stapes		
Height (mm)	1.85	1.54
Width (mm)	1.34	0.95
Angle from Horiz. (°)	39.90	25.50
Ear Canal Opening		
Height (mm)	5.02	4.18
Width (mm)	2.54	2.16
Middle Ear Cavity		
Height (mm)	9.29	7.73
Width (mm)	5.19	7.98

For the adult baboon, the ear canal is both wider and taller than in the newborn. However, the middle ear cavity varies greatly in overall shape between the adult and newborn models. While the adult MEC is taller, it is also significantly narrower than the MEC of the newborn. This gives less room in the anterior-posterior direction for the TM and ossicles.

Orientational differences of the middle ear structures with respect to the middle ear cavity could be due to difference in age besides general growth. Perhaps in the same way that human infants have unfused skull bones, a young baboon's skull hardens at it grows, expanding not only in general size but possibly changing shape of the MEC completely. It is possible this could explain a significantly narrower MEC and a very differently oriented stapes in adulthood.

5.2 Middle Ear Function

Movement of the TM at the umbo is important for understanding sound transmission at is the first transferal of sound waves into vibration before moving down the ossicular chain into the cochlea. FE model sound transmission data both for the young and adult baboon TM umbo movement is shown in Figure 32. The adult values for both FE and experimental mean are higher overall than the newborn values, with the FE values being greater than the experimental mean. On the other hand, the newborn FE model is closer in value to the experimental mean, with a trend of being similar or lower in value than the experimental mean. Deviation from experimental data occurs the most at higher frequencies, beginning at approximately 3500 Hz and increasingly deviating from there.

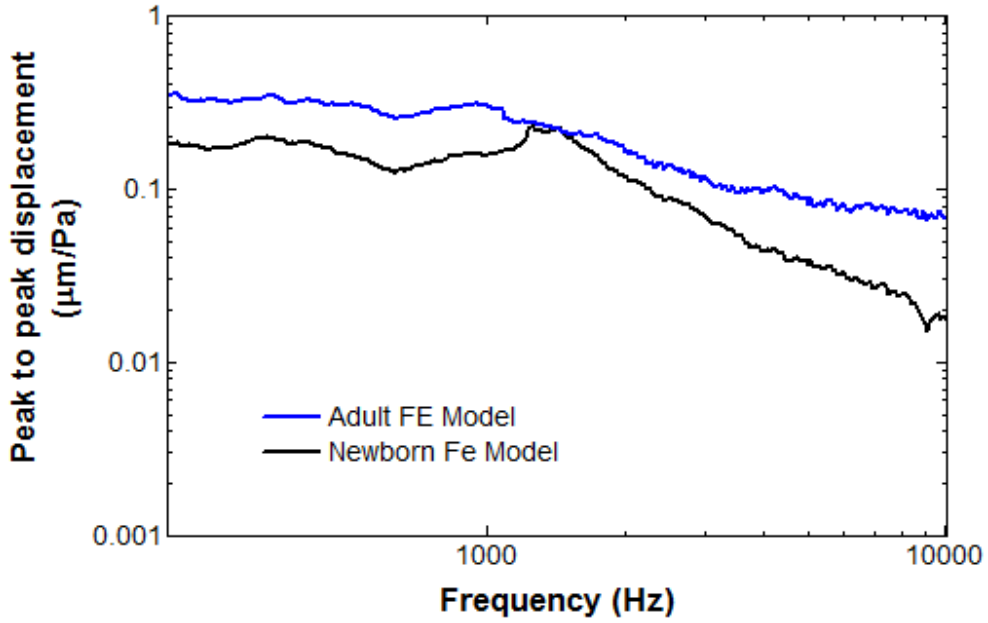

Figure 32. Comparison between adult and newborn FE model sound transmission results.

Even so, the overall shape of the FE curves are similar to those of the experimental groups. At lower frequencies, the curve is flat (note the logarithmic axes) until ~1200 Hz, when the slope increases downward as frequency increases. While the general behavior of the baboon temporal bones has been captured in the FE models, the specific output values are numerically off. This directly points to the idea that having the true values for baboon mechanical properties could help close the gap between the FE model and the experimental data. Furthermore, the experimental sample curves on which the experimental means are based vary significantly, suggesting that the experimental mean could be made more accurate with a higher population size. At this point any potential outliers could be

identified and removed, giving the experimental mean more integrity to serve as a better point of comparison for the FE model.

When only considering the age factor, it is clear from both the experimental means and the model data that the young baboon exhibits lower umbo displacement values during sound transmission than the adult. Experimentally, the young baboon TM moves less at the umbo than the adult TM for 96% of the frequency values. For the FE model, the young baboon TM moves less at the umbo than the adult TM for 99% of the frequency values. Because the newborn TM is thicker than the adult TM, the TM must thin with age. Combined with these findings, it is likely that healthy age-related TM thinning directly contributes to the increase in TM mobility.

5.2.1 Parameter Sensitivity Analysis

Many variables contributed to the accuracy or inaccuracy of the sound transmission analysis results, but certain parameters played a larger role than others. Many analyses were performed by varying specific input values in order to identify which factors carried the largest impact. As expected, mechanical properties of the ossicles played the smallest role in analysis results. Even when varying the values from human to chinchilla bone values (density and stiffness), the bones were still relatively very rigid compared to all other structures in the middle ear. [Note: mechanical properties for the fused chinchilla malleus-incus complex were applied separately to both the malleus and incus for this exercise.] However, material properties for the tendon/ligament boundary conditions played

a larger role in sound transmission results. Of these, the stapeidal annular ligament and the incudostapedial joint were most important. As stiffness of either boundary condition increased, vibration due to sound transmission was reduced causing the mobility of the TM to be subdued. This supports the consensus from previous hearing research with FE models as the movement of the stapes, which is the bone suspended between both of these boundary conditions, the SAL and the ISJ, is considered one of the most important factors besides TM mobility in sound transmission down the ossicular chain.

Finally, after over 30 analyses were performed, TM thickness was determined to have the largest effect on TM umbo displacement during sound transmission. In this thesis, TM thickness was manually measured from fresh temporal bone samples both young and adult for use in the final analysis results. However, if young baboon TMs were immeasurable from lack of availability (young baboon samples are more difficult to obtain) or for any number of reasons, adult and baboon TM thickness would have been assumed equal. Figure 33 demonstrates the decrease in integrity of the FE results when the adult and TM thickness are both considered 25 μm during analysis. While this does not affect the adult FE model results as there is no change in the input values, this does affect the young FE model results.

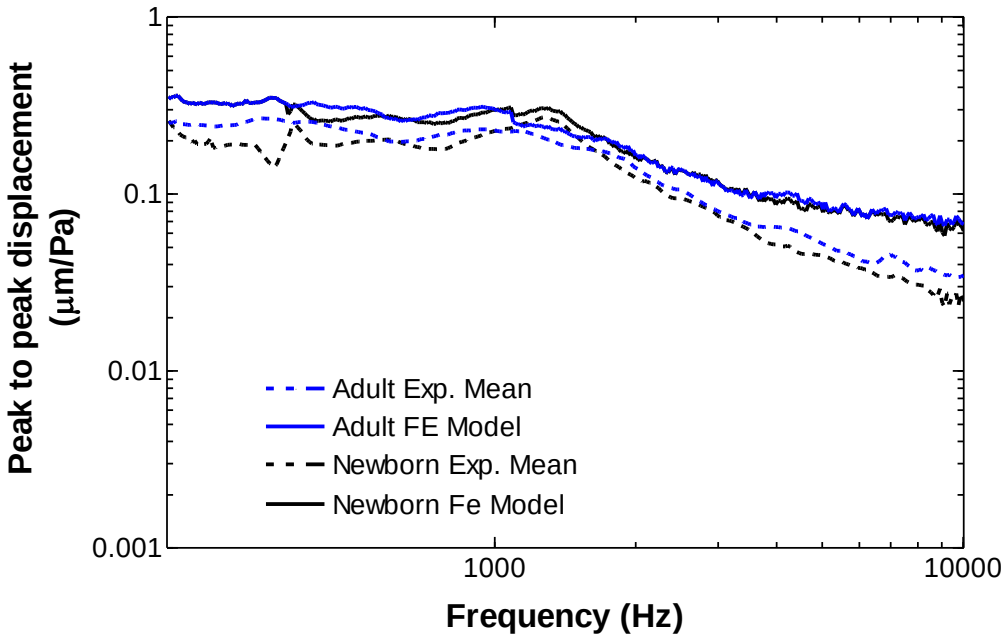

Figure 33. Experimental means for newborn (N=6) and adult (N=6) compared with FE models when TM thickness is assumed to be 25 μm for both adult and newborn FE models.

With TM thickness presumed equal, the FE model results exhibit no age factor; TM umbo mobility in the adult model is very similar to that in the newborn model, particularly for frequency values less than 500 Hz and greater than 1700 Hz. Most importantly, with young TM thickness equal to the measured adult TM thickness, there is significantly less correlation between the newborn FE model and the newborn experimental mean than there is between the two FE models. Accuracy of the TM thickness plays the biggest role in how well the FE model reflects the experimental data.

5.3 Possible Limitations

While all other factors besides age were as controlled as possible, the young baboon was male and the adult baboon was female, meaning any differences discussed in this thesis could be attributed to difference in sex, although that is statistically unlikely for asexual physical characteristics [11]. If the baboon male temporal bone varies greatly from the female temporal bone, this likely a secondary sexual trait, appearing during the transition into sexual maturity. This means the newborn FE model and newborn experimental group should not exhibit any differences due to sex despite being comprised of both sexes because of the young age.

It must also be considered that as they are the first to exist, these baboon middle ear FE models should be considered prototypes. Each was based on one temporal bone and is thus prone to having individual-specific traits that may prevent it from being the optimal representation of the average baboon temporal bone in a particular age group (i.e. very young or adult). Next, these analyses were ran using mechanical property values from human experiments because the mechanical properties for baboon middle ear structures of any age is not yet available. While this research group has explored these values, particularly for the baboon TM, the data is not yet complete enough to have fully defined viscoelastic properties for use in FE analysis. Lastly, the occasionally subjective nature of 3D modeling means there occasionally exists opportunity for human error.

Chapter 6: Conclusion

6.1: Summary of Findings

Micro-Computed Tomography was used to collect cross-sectional images of temporal bones belonging to a newborn male and adult female baboons. Using FEI Amira Software, the images were labelled by structure before the labels were stacked to create 3D computer reconstructions before moving them into Altair HyperMesh for finite element modeling of the middle ear cavity, ear canal, tympanic membrane, ossicles, Eustachian tube opening, round window membrane, and the supporting ligaments and tendons. From here, dimensions were gathered for key components of the adult and newborn baboon ears. Between the adult and young models, major differences were found in shape and size of middle ear cavity, as well as the orientation of the internal structures. Next, Mechanical APDL and ANSYS WorkBench were employed to analyze the fluid and structural dynamics of sound transmission through the ear canal, past the tympanic membrane, down the ossicular chain, and into the stapes footplate. Finally, displacement at the umbo of the tympanic membrane was found using the FE model and validated using laser Doppler vibrometry experimental data for old and young baboon age groups. While the FE models seem to be good representations of their age group, there is room for refinement. Based on these preliminary results, age does seem to play an impact in sound transmission for baboons, with TM mobility increasing with age.

6.2: Moving Forward

As this is the first model its kind, further steps should be taken to improve the reliability and assess the value of the FE baboon middle ear model. First, additional micro-CT scans could be used to increase the sampling size of each 3D model to get a better representation of the newborn and adult ears. This could help elucidate the effect age has on both the structure and function of the baboon ear. Furthermore, a larger group would account for and/or highlight any variations in structure possibly due to sex. Next, the investigation into the mechanical properties of the baboon ear structures would allow FE analyses to be ran using baboon data instead of human data to get a more accurate representation of how sound transmits through the ear. This research group is already working towards this particular goal. Finally, ideally after the above steps are taken, displacement of the stapes footplate with sound transmission could be analyzed to gain better understanding of the relationship between the middle ear and the cochlea, which houses the hair cells that allow for the sensation of hearing.

References

[1] Dormehl, I. C., N. Hugo, and G. Beverley. “The Baboon: An Ideal Model in Biomedical Research.” *Anesthesia & Pain Control in Dentistry* 1, no. 2 (1992): 109–15.

[2] Schilder, Anne G. M., Tal Marom, Mahmood F. Bhutta, Margaretha L. Casselbrant, Harvey Coates, Marie Gisselsson-Solén, Amanda J. Hall, et al. “Panel 7: Otitis Media: Treatment and Complications.” *Otolaryngology--Head and Neck Surgery: Official Journal of American Academy of Otolaryngology-Head and Neck Surgery* 156, no. 4_suppl (April 2017): S88–105.

[3] Grow, Douglas A., John R. McCarrey, and Christopher S. Navara. “Advantages of Nonhuman Primates as Preclinical Models for Evaluating Stem Cell-Based Therapies for Parkinson’s Disease.” *Stem Cell Research* 17, no. 2 (September 2016): 352–66.

[4] Nyachieo, Atunga, Daniel C. Chai, Jan Deprest, Jason M. Mwenda, and Thomas M. D’Hooghe. “The Baboon as a Research Model for the Study of Endometrial Biology, Uterine Receptivity and Embryo Implantation.” *Gynecologic and Obstetric Investigation* 64, no. 3 (2007): 149–55.

[5] Fazleabas, A. T., J. J. Kim, S. Srinivasan, K. M. Donnelly, A. Brudney, and R. C. Jaffe. “Implantation in the Baboon: Endometrial Responses.” *Seminars in Reproductive Endocrinology* 17, no. 3 (1999): 257–65.

[6] Wright, C. G., A. R. Halama, and W. L. Meyerhoff. “Ototoxicity of an Ototopical Preparation in a Primate.” *The American Journal of Otology* 8, no. 1 (January 1987): 56–60.

[7] Wright, C. G., W. L. Meyerhoff, and A. R. Halama. “Ototoxicity of Neomycin and Polymyxin B Following Middle Ear Application in the Chinchilla and Baboon.” *The American Journal of Otology* 8, no. 6 (November 1987): 495–99.

[8] Martin, G. K., B. L. Lonsbury-Martin, R. Probst, and A. C. Coats. “Spontaneous Otoacoustic Emissions in the Nonhuman Primate: A Survey.” *Hearing Research* 20, no. 1 (1985): 91–95.

[9] Geyer, G., and J. Helms. “[Ionomer Cement Prostheses in Reconstructive Middle Ear Surgery].” *HNO* 45, no. 6 (June 1997): 442–47.

[10] Moore, J. K., K. K. Osen, J. Storm-Mathisen, and O. P. Ottersen. “Gamma-Aminobutyric Acid and Glycine in the Baboon Cochlear Nuclei: An Immunocytochemical Colocalization Study with Reference to Interspecies Differences in Inhibitory Systems.” *The Journal of Comparative Neurology* 369, no. 4 (June 10, 1996): 497–519.

[11] Lockwood, Charles A, John M Lynch, and William H Kimbel. “Quantifying Temporal Bone Morphology of Great Apes and Humans: An Approach Using Geometric Morphometrics.” *Journal of Anatomy* 201, no. 6 (December 2002): 447–64.

[12] Wang, Xuelin, and Rong Z. Gan. “3D Finite Element Model of the Chinchilla Ear for Characterizing Middle Ear Functions.” *Biomechanics and Modeling in Mechanobiology* 15, no. 5 (October 2016): 1263–77.

[13] Chen, Yongzheng, Xiying Guan, Tianyu Zhang, and Rong Z. Gan. “Measurement of Basilar Membrane Motion during Round Window Stimulation in Guinea Pigs.” *Journal of the Association for Research in Otolaryngology: JARO* 15, no. 6 (December 2014): 933–43.

[14] Montealegre-Z, Fernando, and Daniel Robert. “Biomechanics of Hearing in Katydids.” *Journal of Comparative Physiology. A. Neuroethology, Sensory, Neural, and Behavioral Physiology* 201, no. 1 (January 2015): 5–18.

[15] Ginat, Daniel Thomas, and Rajiv Gupta. “Advances in Computed Tomography Imaging Technology.” *Annual Review of Biomedical Engineering* 16 (July 11, 2014): 431–53.

[16] Wang, Xuelin, Xiying Guan, Mario Pineda, and Rong Z. Gan. “Motion of Tympanic Membrane in Guinea Pig Otitis Media Model Measured by Scanning Laser Doppler Vibrometry.” *Hearing Research* 339 (September 2016): 184–94.

[17] Smeak, Daniel D. “Treatment of Persistent Deep Infection After Total Ear Canal Ablation and Lateral Bulla Osteotomy.” *The Veterinary Clinics of North America. Small Animal Practice* 46, no. 4 (July 2016): 609–21.

[18] Gan, Rong Z., Fan Yang, Xiangming Zhang, and Don Nakmali. “Mechanical Properties of Stapedial Annular Ligament.” *Medical Engineering & Physics* 33, no. 3 (April 2011): 330–39.

[19] Hitt, Brooke M., Xuelin Wang, and Rong Z. Gan. “Dynamic Property Changes in Stapedial Annular Ligament Associated with Acute Otitis Media in the Chinchilla.” *Medical Engineering & Physics* 40 (February 2017): 65–74.

[20] Gan, Rong Z., Don Nakmali, Xiao D. Ji, Kegan Leckness, and Zachary Yokell. “Mechanical Damage of Tympanic Membrane in Relation to Impulse Pressure Waveform - A Study in Chinchillas.” *Hearing Research* 340 (October 2016): 25–34.

[21] R. Gan, B. Feng and Q. Sun, "3-Dimensional Finite Element Modeling of Human Ear for Sound Transmission." *Annals of Biomedical Engineering*, vol. 32, no. 6, (2004): 847-856.

[22] X. Wang, T. Cheng and R. Gan, "Finite-Element Analysis of Middle-Ear Pressure Effects on Static and Dynamic Behavior of the Human Ear." *The Journal of the Acoustic Society of America*, vol. 122, no. 2, (2007): 906-917.

[23] R. Gan, B. Reeves and X. Wang, "Modeling of Sound Transmission from Ear Canal to Cochlea." *Annals of Biomedical Engineering*, vol. 35, no. 12, (2007): 2180-2194.

[24] R. Gan, T. Cheng, C. Dai and F. Yang, "Finite Element Modeling of Sound Transmission with Perforations of Tympanic Membrane." *The Journal of the Acoustic Society of America*, vol. 126, no. 1, (2009): 243-253.

[25] X. Zhang and R. Gan, "Finite Element Modeling of Energy Absorbance in Normal and Disordered Human Ears." *Hearing Research*, vol. 301, (2013): 146-155.

[26] R. Gan, M. Wood and e. al., "A Totally Implantable Hearing System - Design and Function Characterization in a 3D Computational Model and Temporal Bones." *Hearing Research*, vol. 263, no. 1-2, (2010): 138-144.

[27] T. Koike, H. Wada, and T. Kobayashi, “Modeling of the Human Middle Ear Using the Finite-Element Method.” *The Journal of the Acoustic Society of America*, vol. 111, no. 3, (March 2002): 1306–1317.

[28] R. Z. Gan, D. Nakmali, X. D. Ji, K. Leckness, and Z. Yokell, “Mechanical Damage of Tympanic Membrane in Relation to Impulse Pressure Waveform – A Study in Chinchillas.” *Hearing Research*, vol. 340, (October 2016): 25–34.

[29] G. Viallet, G. Sgard, F. Laville and J. Boutin, "Axisymmetic versus Three-Dimensional Finite Element Models for Predicting the Attenuation of Earplugs in Rigid Walled Ear Canals." *The Journal of the Acoustic Society of America*, vol. 134, no. 6, (2003): 4470-4480.

[30] Jiang, Shangyuan, Thomas W. Seale, and Rong Z. Gan. “Morphological Changes in the Round Window Membrane Associated with Haemophilus Influenzae-Induced Acute Otitis Media in the Chinchilla.” *International Journal of Pediatric Otorhinolaryngology* 88 (September 2016): 74–81.

[31] Jia, Xu, Shenghui Liao, Xuanchu Duan, Wanqiu Zheng, and Beiji Zou. “Anisotropic Finite Element Modeling Based on a Harmonic Field for Patient-Specific Sclera.” *BioMed Research International* 2017 (2017): 6073059.

[32] Koike, Takuji, Hiroshi Wada, and Toshimitsu Kobayashi. “Modeling of the Human Middle Ear Using the Finite-Element Method.” *The Journal of the Acoustical Society of America* 111, no. 3 (March 2002): 1306–17.

[33] Ling, Zhao, Yang Liyuan, Liu Cuiling, and Gao Xu. “[Three-dimensional finite element analyses of the deep wedge-shaped defective premolars restored with different methods].” *Hua Xi Kou Qiang Yi Xue Za Zhi = Huaxi Kouqiang Yixue Zazhi = West China Journal of Stomatology* 35, no. 1 (February 1, 2017): 77–81.

[34] Lockwood, Charles A, John M Lynch, and William H Kimbel. “Quantifying Temporal Bone Morphology of Great Apes and Humans: An Approach Using Geometric Morphometrics.” *Journal of Anatomy* 201, no. 6 (December 2002): 447–64.

[35] Zhang X, RZ Gan. “A Comprehensive Model of Human Ear for Analysis of Implantable Hearing Devices.” *IEEE Transactions on Biomedical Engineering* 58(10) (October 2011): 3024-7.

[36] Guan, Xiying, Shangyuan Jiang, Thomas W. Seale, Brooke M. Hitt, and Rong Z. Gan. “Morphological Changes in the Tympanic Membrane Associated with Haemophilus Influenzae-Induced Acute Otitis Media in the Chinchilla.” *International Journal of Pediatric Otorhinolaryngology* 79, no. 9 (September 2015): 1462–71.

[37] Plessis, AD, C Broeckhoven, A Guelpa, S Gerhard le Roux. “Laboratory X-ray Micro-Computed Tomography: A User Guideline for Biological Samples.” *Gigascience* 2017 (April 2017).

Appendix A: List of Acronyms

C1	Superior Malleolar Ligament
C2	Lateral Malleolar Ligament
C3	Posterior Incudal Ligament
C4	Anterior Malleolar Ligament
C5	Posterior Stapedial Tendon
C7	Tensor Tympani Tendon
CAD	Computer Aided Design
FE	Finite Element
FSI	Fluid-Structure Interaction/Interaction
IMJ	Incudomalleolar Joint
ISJ	Incudostapedial Joint
LDV	Laser Doppler Vibrometry
ME	Middle Ear
OCT	Optical Coherence Tomography
SAL	Stapedial Annular Ligament
SLDV	Scanning Laser Vibrometry
SPL	Sound Pressure Level
TB	Temporal Bone
TM	Tympanic Membrane